On the modelling of shallow turbidity flows

Valery Liapidevskii, Denys Dutykh, Marguerite Gisclon

Valery Liapidevskii
Lavrentyev Institute of Hydrodynamics, Novosibirsk, Russia
Novosibirsk State University, Novosibirsk, Russia

Denys Dutykh
CNRS–LAMA, Université Savoie Mont Blanc, France

Marguerite Gisclon
LAMA, Université Savoie Mont Blanc, France

On the modelling of shallow turbidity flows

arXiv.org / HAL

Last modified: April 25, 2017

On the modelling of shallow turbidity flows

Valery Yu. Liapidevskii, Denys Dutykh*, and Marguerite Gisclon

Abstract. In this study we investigate shallow turbidity density currents and underflows from mechanical point of view. We propose a simple hyperbolic model for such flows. On one hand, our model is based on very basic conservation principles. On the other hand, the turbulent nature of the flow is also taken into account through the energy dissipation mechanism. Moreover, the mixing with the pure water along with sediments entrainment and deposition processes are considered, which makes the problem dynamically interesting. One of the main advantages of our model is that it requires the specification of only two modeling parameters — the rate of turbulent dissipation and the rate of the pure water entrainment. Consequently, the resulting model turns out to be very simple and self-consistent. This model is validated against several experimental data and several special classes of solutions (such as travelling, self-similar and steady) are constructed. Unsteady simulations show that some special solutions are realized as asymptotic long time states of dynamic trajectories.

Key words and phrases: turbidity currents; density flows; shallow water flows; conservation laws; finite volumes; travelling waves; self-similar solutions

MSC: [2010] 76T10 (primary), 76T30, 65N08 (secondary)
PACS: [2010] 47.35.Bb (primary), 47.55.Hd, 47.11.Df (secondary)

Key words and phrases. turbidity currents; density flows; shallow water flows; conservation laws; finite volumes; travelling waves; self-similar solutions.

* Corresponding author.

Contents

1. Introduction

Underwater turbidity currents are sediment-laden underflows that play an important rôle in the morphology of the continental shelves (more generally of ocean bottoms) and in the global sediment cycle going to the formation of hydrocarbon reservoirs. We refer to [117] for a self-contained and comprehensive account of the theory of gravity currents and intrusions. The presence and entrainment of sediments differentiates them from stratified flows due to, *e.g.* temperature or salinity differences. The main physical mechanisms include the deposition, erosion and dispersion of important amounts of heavy sediment particles. Turbidity currents are not to be confused with *debris flows*, which represent fast-moving masses of poorly sorted heterogeneous material where interactions among the material pieces ($\approx$ particles) are important. Moreover, debris mix little with the ambient fluid. Debris flows have been a mainstream topic in the scientific literature due to their hazard they wreak in mountain regions (and not only).

The driving force is the gravity acceleration acting on dispersed sediment particles along steep and moderate bottom slopes. The initial perturbation is amplified by this acceleration, which in turn destabilizes the flow into shear instabilities that result in turbulent mixing and the transfer of mass and momentum. This gravity force creates the horizontal pressure gradient due to the increase of hydrostatic pressure resulting from the addition of particles. The heavy sediment particles are suspended in the mixing layer by fluid turbulence. The studied here processes are responsible of the transfer of littoral sediments to deep ocean regions. One should not disregard the destructive potential of gravity currents onto underwater structures such as pipelines, cables, *etc.*Turbidity currents in submarine canyons can attain surprisingly high velocities of the order of $\approx$ 8 $\sim$ 14 m/s [67, 98]. These high velocities in the downstream direction result from the self-acceleration (and self-suspension) process from an appropriate initial perturbation, when more and more sediments are entrained by the flow from the bed, thus, increasing the rate of work performed by gravity [98]. This process is sometimes referred to as the "ignition" [44, 97, 98], which translates the energy imbalance property of such flows. One of important scientific questions is to determine the conditions necessarily to have an igniting flow. However, the self-acceleration stage cannot continue indefinitely. Most often the bed slope drops off (due to the bed morphology) or, simply, the sediment supply ceases. The mechanism of ignition was already described in Pantin (1979) [96]. However, the first laboratory demonstration of self-accelerated turbidity flows took 30 more years [108].

Turbidity currents is a particular case of (continuously) stratified flows and they are fundamentally different from classical density underflows [33]. The main difference comes from the fact that the source of the density gradient, *i.e.* the suspended sediment, is not conservative. The suspended sediments are free to exchange with the core layer near the sea bed. The ambient still water is also entrained into this process. These exchanges are difficult to quantify and they constitute one of the main difficulties in the modeling of such flows [96–98]. In this respect turbidity currents are fundamentally non-conservative flows

in their nature. Gravity flows may occur in the atmosphere* over topography, sub-aerial (*e.g.* avalanches, pyroclastic flows) and sub-aqueous environments (*e.g.* turbidity currents) over bathymetries. They may result also from anthropogenic activities such as when a dense buoyant industrial effluent or pollutant is released into a lake, river or ocean. In the present study we shall consider mainly sub-aqueous flows due to the abundance of available experimental data. We refer to [83, 99] as general excellent reviews on this topic.

Perhaps, the first serious attempts to observe turbidity currents in natural environments were performed in late 1960's at Scripps Canyon offshore of La Jolla, California. They were reported in [60]. However, the flows reported in that study were so violent that the instrumentation was lost during these density currents making the detailed analysis extremely difficult [99]. The exact time moment of these underwater events is unpredictable which make them difficult to monitor in natural environments. Most of our physical knowledge on underwater turbidity currents come from small scale laboratory experiments [44, 68, 69, 86]. The experiments are bound to use common liquids for practical reasons. In general, it is not possible to respect all scalings. To give an example, we can mention the issue with particle sizes and their settling velocity. Nevertheless, taking into account the difficulties in obtaining field data, laboratory experiments are the only source of quantitative data about turbidity currents. The mathematical modelling is needed to extrapolate these experimental results to the scales on which these processes occur in nature. Nonetheless, the experiments offer a great opportunity for the verification of numerical results.

The same processes take place on somehow smaller scales in the lakes as well. The first recognition of the rôle of turbidity currents in limnology goes back to Forel (1885) [42], who conjectured that a sub-aqueous canyon in Lake Geneva had been created by underflows from the Rhône river. This process was investigated experimentally in [70], which is the first experimental study of density currents to our knowledge. Thus, Kuenen (1938) [70] recognized scientifically their potential importance in the transport of sediments. Turbidity currents and underwater landslides are the principal natural mechanisms of sediment transport from shallow to deep waters. Transport distances range from hundred meters to hundred kilometers for Ocean bottoms. This distance is generally referred as the *run-out*. Erosion and deposition by turbidity currents are responsible for numerous features observable on the Ocean bottom. Moreover, we know today that many hydrocarbon reservoirs consist of turbidity current deposits.

The present study was conducted at the University Savoie Mont Blanc's Campus near from the Lake Le Bourget, the biggest natural lake in France. For instance, the sedimentary depositions in Alpine lakes have been studied recently [8, 20, 21]. In the same time the water circulation and currents in the Lake Léman (also known as Lake of Geneva) have been measured recently using a submarine [37–39]. The results presented in this study could be applied to some aspects of the limnology as well where the stratified density flows may appear. In natural environments, sub-aqueous sediment

*For instance, downslope windstorms over topography in Colorado (US) were observed and examined in [76, 91].

gravity flow domain can be conventionally divided into three dynamically distinct regions in the evolution of a downslope current along a slope:

(1) Source region, where the flow is originated
(2) Transfer region, where the flow accelerates
(3) Deposition region, where the flow decelerates and suspended sediments settle down on the bed.

The gravity current can be divided geometrically into the flow *head*, *body* and *tail*. The head is shaped as an ellipse and, generally the head is higher than the flow body. In the present study we are mainly interested in the flow head modelling, where the most intensive mixing processes take place. Consequently, it influences the whole flow dynamics. The most advanced point of the flow head is called the front or nose.

The main difficulties in understanding the dynamics of gravity turbidity currents come from their genuinely turbulent nature. Moreover, the phenomenon is nonlinear, heterogeneous and unsteady. The flow complexity increases when the flow entrains more and more sediments in suspension. The literature devoted to the mathematical modeling of the density currents is abundant. First of all, we would like to mention the classical monographs on this subject [75, 113, 115]. The first and simplest models intended to explain the classical lock-exchange configurations was proposed in [58]. These models are referred to as *integral*, *box* or 0D models, since all quantities are averaged in space. The modern approaches to the mathematical modeling of such flows were initiated in [96–98]. A dense cloud 0D model for powder-snow avalanches including non-BOUSSINESQ and sediment entrainment effects along the avalanche path was proposed in [103]. Powder-snow avalanches are large-scale, finite volume release turbidity currents (in the form of large scale suspension clouds) occurring on mountain slopes. These clouds sometimes reach 100 m in height and the front velocities of the order of 100 $\frac{\mathsf{m}}{\mathsf{s}}$. Without sediments (*i.e.* snow in the case of avalanches) distributed over the incline, the density current first accelerates and then decelerates without reaching important velocities. With sediments entrainment, the current can be maintained in the accelerating self-sustaining state during sufficient intervals of time to reach the velocities indicated above. In [56] a fair correlation of the avalanche velocity with the snow cover was demonstrated. The measurements of an avalanche front velocity in the SION valley, SWITZERLAND demonstrate a constant increase of the front velocity with traveled distance [27]. Thus, we come to the conclusion that the inclusion of sediments entrainment effect is of capital importance to predict the correct density current front velocity.

Some of recent studies devoted to the sediments transport within depth-averaged models include [10–12, 16, 40, 66, 88]. This list is far from being exhaustive. The shallow water approach assumes that vertical accelerations are negligible, so the pressure being essentially hydrostatic. The sediment concentration is a passive tracer with exchanges among different layers. The flow is fully turbulent, even if pure viscous effects are generally negligible. Moreover, the energy required to keep the sediments in the suspension cloud is a negligible portion of the total turbulent energy production [98]. Thus, the base model has to be first REYNOLDS-averaged [109] before applying the long wave approximation. Several

authors made an effort to take into account the turbulence modeling into the shallow water type models [35, 36, 82]. Our approach to solve this issue will be detailed below. Nowadays, the multi-layer approaches to the density stratified flows become more and more popular [5]. Finally, some researchers chose a more CFD*-like approach to the simulation of density flows incorporating eventually the advanced turbulence modeling [13, 34, 94, 95]. Perhaps, the first Direct Numerical Simulation (DNS) of the gravity current dates back to the year of 2 000 [54]. These simulations have an advantage of being depth-resolving and, thus, providing very a complete information about the flow structure in two or even three dimensions. However, due to the high computational complexity, only idealized academic configurations can be considered within reasonable CPU-time at the current state of technologies. Recently proposed three-dimensional (3D) turbidity-current models can be found in [57, 59, 64]. Moreover, the 3D DNS computations are often limited in the bulk Reynolds number.

In the present study we adopt a simplified (1.5D) approach along the lines of [23, 74, 107] based on the Eulerian formulation and depth-averaged formulations. A Lagrangian simplified BANG1D model was proposed in [102]. A simple 1.5D model was proposed in [62]. The authors parametrized their model by making the entrainment velocity depending on the dimensionless Richardson number. In the present study we close the model in an alternative way.

Very similar physical processes take place in powder-snow avalanches where the snow particles suspension flows down the mountains and the snow plays the rôle of sediments in underflows [56]. Consequently, very similar mathematical models appear in these two fields and to make the bibliography review more complete we mention some recent results in powder-snow avalanche modeling [3, 4, 14, 28, 34, 84, 89, 114].

The goal here is to propose a simple multi-layer (just two or three layers) shallow water-type model which takes into account mixing processes between the layers. We assume that the sediment particles are well mixed across the height of each layer. So that their volume fraction can be effectively approximated by depth-averaged quantities. This model preferably has to be simple enough to be studied using even analytical methods. The main scientific question which is currently poorly understood is the influence of flow stratification on global flow patterns. For instance, the formation of current's head (or the front region) and its steady-state velocity have to be carefully explained [74].

The present study is organized as follows. In Section 2 we state the physical and mathematical problem under consideration. In Section 3 we study the derived model analytically and in Section 4 we validate its predictions by comparing them against experimental data. Some unsteady simulations and their relation to analytical (self-similar) solutions are presented in Section 4 as well. Finally, the main conclusions and perspectives of this study are outlined in Section 5.

*Computational Fluid Dynamics (CFD).

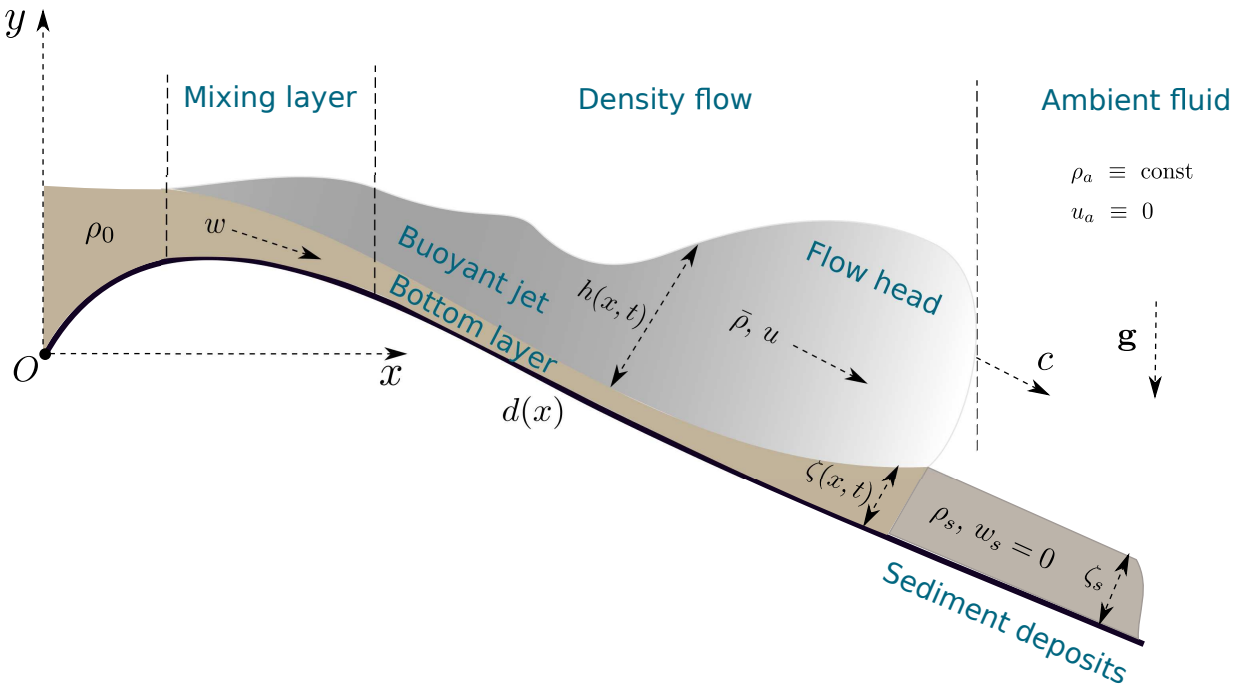

Figure 1. *Sketch of the physical domain and the flow configuration. Various notations and variables are introduced and explained in the text.*

2. Mathematical model

Consider an incompressible liquid which fills a two-dimensional fluid domain Ω. A Cartesian coordinate system $O\boldsymbol{x}$, $\boldsymbol{x} = (x, y)$ is chosen in a classical way such that the axis Oy points vertically upward and abscissa Ox is positive along the right horizontal direction. The fluid is bounded below by a solid non-erodible bottom $y = d(x)$. Above, the fluid can be assumed unbounded for the sake of simplicity, since our attention will be focused on processes taking place in the region close to the bottom.

The fluid is inhomogeneous and the flow can be conventionally divided in three parts. On the solid bottom there is a heavy fluid layer with density ρ_0 composed mainly of sedimentary deposits. Its thickness is $\zeta(x, t)$. Above, we have a muddle layer whose density will be denoted by $\bar{\rho}(\boldsymbol{x}, t)$ composed of the sediments and the still water mix. Its thickness is $h(x, t)$. Finally, the whole domain above these two layers is filled with the still ambient water of the density $\rho_a > 0$ at rest ($\boldsymbol{u}_a \equiv \boldsymbol{0}$). This situation is schematically depicted in Figure 1. We include also into consideration the situation where a thin motionless layer of sediments with constant thickness ζ_s and density $\rho_s > 0$ covers the slope. It is usually the case in many practical situations and these sediment deposits may contribute to the flow head dynamics while propagating along the incline. One may imagine also that a certain mass of a sediment suspension or dense fluid is released into the flow domain at $y = 0$ with the mass flux $\rho_0 \cdot \zeta(0, t) \cdot u(0, t)$.

Remark 1. *L.* Ovsyannikov *(1979) showed [93] that the quiescent still water layer can be indifferently chosen to have a free surface or to be bounded above by a rigid wall. Some authors assume the latter case [24, 88]. Both boundary conditions lead to the same mathematical long wave model under the* Boussinesq *assumption** *which will be adopted below. So, in the present study for the sake of convenience we choose the infinite still water layer.*

If we assume the fluid to be perfect, its flow can be described by classical incompressible Euler equations. The variable fluid density $\rho(\boldsymbol{x}, t)$ and the fluid velocity field $\boldsymbol{u}(\boldsymbol{x}, t) \stackrel{\text{def}}{:=} \big(u(\boldsymbol{x}, t),\, v(\boldsymbol{x}, t)\big)$ satisfy the following system of equations:

$$\begin{aligned} \boldsymbol{\nabla} \cdot \boldsymbol{u} &= 0\,, \\ \rho_t \,+\, \boldsymbol{\nabla} \cdot [\,\rho\, \boldsymbol{u}\,] &= 0\,, \\ (\rho\, \boldsymbol{u})_t \,+\, \boldsymbol{\nabla} \cdot [\,\rho\, \boldsymbol{u} \otimes \boldsymbol{u} \,+\, p\, \mathbb{I}\,] &= \rho\, \mathbf{g}\,, \end{aligned}$$

where the subscript t denotes the differentiation with respect to time and the operator $\boldsymbol{\nabla} \stackrel{\text{def}}{:=} (\partial_x,\, \partial_y)$ is the gradient, $p\,(\boldsymbol{x}, t)$ is the fluid pressure variable and $\mathbb{I} \,=\, (\delta_{ij})_{1 \leqslant i,\, j \leqslant 2}$ is the identity tensor compactly written with the Kronecker δ-operator. Taking into account the choice of the coordinate system, the gravity acceleration vector is directed vertically downwards, *i.e.* $\mathbf{g} \,=\, (0,\, -g)$. The ideal fluid assumption can be also seen as a flow with an infinitely large Reynolds number $\mathrm{Re} \,\to\, +\infty$ [71, 110]. So, the flow is a priori turbulent and we shall return to this question below.

In sediment gravity flows the particle (sediment) density is generally larger, but still of the same order of magnitude as the ambient fluid. Thus, in turbidity flows modeling it is common to assume that the density variations inside the fluid column are not large, *i.e.*

$$\frac{\rho_0 \,-\, \rho_a}{\rho_a} \,\ll\, 1\,. \tag{2.1}$$

In these conditions the so-called Boussinesq approximation can be applied [43, 90], which consists in taking into account the density variations only in the buoyancy term. This approximation results in the following system of equations:

$$\boldsymbol{\nabla} \cdot \boldsymbol{u} = 0\,, \tag{2.2}$$

$$b_t \,+\, \boldsymbol{\nabla} \cdot [\,b\, \tilde{\boldsymbol{u}}\,] = 0\,, \tag{2.3}$$

$$\boldsymbol{u}_t \,+\, \boldsymbol{\nabla} \cdot \Big[\, \boldsymbol{u} \otimes \boldsymbol{u} \,+\, \frac{p}{\rho_a}\, \mathbb{I}\,\Big] = \boldsymbol{b}\,, \tag{2.4}$$

where for the sake of convenience we replace the density variations $\dfrac{\rho \,-\, \rho_a}{\rho_a}$ by the so-called buoyancy function b:

$$b\,(\boldsymbol{x},\, t) \stackrel{\text{def}}{:=} \frac{\rho \,-\, \rho_a}{\rho_a}\, g\, \pi\,(\boldsymbol{x},\, t)\,, \qquad \boldsymbol{b}\,(\boldsymbol{x},\, t) \stackrel{\text{def}}{:=} \big(0,\, -b\,(\boldsymbol{x},\, t)\big)\,.$$

*In turbidity density currents the particle concentrations are in general sufficiently low (with 0.1 – 7% of the volume [83]). In such concentrations particle/particle interactions are negligible [6]. Thus, from the modelling point of view the Boussinesq approximation is generally adopted.

We note that the variable density in the flow can be realized by the variable concentration of sediments or by dense fluid input. The function $\pi(\boldsymbol{x}, t)$ is the concentration of the sediments in the suspension [25, 61, 84]. For instance, the concentration $\pi(\boldsymbol{x}, t)$ is equal identically to zero in the still pure water region and it is equal to one in the bottom sediments layer. However, sometimes the sediments porous nature needs to be taken into account [32, 52, 85, 92, 104]. In our modeling paradigm it can be achieved through choosing the concentration value $\pi(\boldsymbol{x}, t) \equiv \pi_0 \lesssim 1$ in the sedimentary layer slightly smaller than one.

Remark 2. *Earlier we introduced the buoyancy $b(\boldsymbol{x}, t)$ through the variable concentration of sediments. However, this quantity can be introduced independently of the physical mechanism, which creates the density gradient. For instance, the density current can be created by injecting a heavy fluid into the light ambient. In this case the quantity $\pi(\boldsymbol{x}, t)$ should be understood as the heavy fluid volumetric concentration.*

Finally, the buoyancy transport velocity $\tilde{\boldsymbol{u}}$ incorporates the sediment fall velocity v_s, which is assumed to be constant in our study:

$$\tilde{\boldsymbol{u}} \stackrel{\text{def}}{:=} (u,\ v - v_s).$$

Some empirical consideration about the determination of the parameter v_s can be found in [26], for example. System (2.2) – (2.4) possesses an energy conservation law which can be readily obtained:

$$\left(\tfrac{1}{2}|\boldsymbol{u}|^2 + b\,y\right)_t + \boldsymbol{\nabla}\cdot\left[\left(\tfrac{1}{2}|\boldsymbol{u}|^2 + b\,y\right)\boldsymbol{u} + \frac{p\,\boldsymbol{u}}{\rho_a}\right] = y\,(b\,v_s)_y, \tag{2.5}$$

where $|\boldsymbol{u}|^2 \equiv u^2 + v^2$ denotes the usual EUCLIDEAN distance. The subscript $(\cdot)_y$ in the right hand side denotes the partial derivative with respect to y. We underline the fact that Equation (2.5) is a direct differential consequence of the governing equations (2.2) – (2.4). So, up to this point equation (2.5) is redundant.

Remark 3. *In the description of density currents some important quantities are traditionally introduced. For instance, one can consider the* effective *gravitational acceleration [115]:*

$$\tilde{g} \stackrel{\text{def}}{:=} g\,\frac{\rho_0 - \rho_a}{\rho_a} \equiv g\,\frac{\Delta\rho}{\rho_a}.$$

Then, the densiometric FROUDE *number can be defined:*

$$\mathrm{Fr_d} \stackrel{\text{def}}{:=} \frac{u}{\tilde{g}\,h\,\cos\varphi},$$

where h is the characteristic height of the density current and u is the typical flow velocity. The FROUDE *number is a dimensionless quantity, which expresses the relative importance of buoyancy and inertia.*

Finally, the RICHARDSON *number can be also introduced [115]:*

$$\mathrm{Ri} \stackrel{\text{def}}{:=} \frac{1}{\mathrm{Fr_d^2}} = \frac{\tilde{g}\,h\,\cos\varphi}{u^2}.$$

For example, based on extensive experimental observations, Keulegan *(1957) [65] derived a simple equation to estimate the head velocity:*

$$U_f \;\approx\; C_K \sqrt{\tilde{g}\, h_f}\,,$$

where C_K *is a constant belonging to the range* $0.7 \;\sim\; 0.9$ *and* h_f *is the flow head height.*

One could also introduce the so-called Péclet *number, which measures the relative importance of advective effects to the solute* diffusion. However, along with the* Reynolds *number this parameter is extremely large and, thus, of little help.*

Early mathematical models used simple empirical relations to parametrize mixing across the interfaces. These relations have typically been based on the Richardson *number [33]. Recently, a simple shallow water model was augmented with an empirical experiment-based entrainment rate relation involving the* Richardson *number [62]. Taking into account that* Reynolds *and* Péclet *numbers are huge for turbidity currents, the* Richardson *number is the only primary parameter for this type of flows. We note also that below we use rather its* alter ego — *the* Froude *number.*

This remark partially explains the importance of various dimensionless numbers in the modeling of turbidity density currents.

The flow under consideration is clearly turbulent and we are going to take into account this fact into our model. Namely, we apply the classical Reynolds decomposition of all the fields present in our model into the mean and fluctuating parts [2, 53, 109]:

$$\boldsymbol{u} \;\longrightarrow\; \boldsymbol{u} \;+\; \boldsymbol{u}', \qquad p \;\longrightarrow\; p \;+\; p', \qquad b \;\longrightarrow\; b \;+\; b'\,,$$

where for the sake of compactness we denote the average part by the same symbol, while the fluctuations are denoted with primes. After substituting this decomposition into the governing equations (2.2) – (2.4) and applying an averaging operator [78, 109], we obtain the following Reynolds averaged version of the model:

$$\boldsymbol{\nabla}\cdot\boldsymbol{u} \;=\; 0\,, \tag{2.6}$$

$$b_t \;+\; \boldsymbol{\nabla}\cdot\left[\, b\,\tilde{\boldsymbol{u}} \;+\; \overline{b'\,\boldsymbol{u}'}\,\right] \;=\; 0\,, \tag{2.7}$$

$$\boldsymbol{u}_t \;+\; \boldsymbol{\nabla}\cdot\Big[\,\boldsymbol{u}\otimes\boldsymbol{u} \;+\; \overline{\boldsymbol{u}'\otimes\boldsymbol{u}'} \;+\; \frac{p}{\rho_a}\,\mathbb{I}\,\Big] \;=\; \boldsymbol{b}\,, \tag{2.8}$$

where the over bar denotes the classical Reynolds average [106]. The same decomposition and averaging operations can be applied to the energy conservation equation (2.5):

$$\Big(\tfrac{1}{2}\,(|\,\boldsymbol{u}\,|^2 \;+\; q^2) \;+\; b\,y\Big)_t \;+\; \boldsymbol{\nabla}\cdot\left[\,\Big(\tfrac{1}{2}\,(\,|\boldsymbol{u}|^2 \;+\; q^2) \;+\; b\,y\Big)\,\boldsymbol{u} \;+\; \frac{p}{\rho_0}\,\mathbb{I}\,\right] \;+$$

$$+\;\boldsymbol{\nabla}\cdot\left[\,\overline{\boldsymbol{u}'\otimes\boldsymbol{u}'}\,\boldsymbol{u} \;+\; y\,\overline{b'\,\boldsymbol{u}'} \;+\; \frac{\overline{p'\,\boldsymbol{u}'}}{\rho_a} \;+\; \overline{|\,\boldsymbol{u}'\,|^2\,\boldsymbol{u}'}\,\right] \;=\; y\,(b\,v_s)_y\,, \tag{2.9}$$

*It could be also the thermal diffusion in other problems, see [22].

where $q \stackrel{\text{def}}{:=} |\boldsymbol{u}'|$ is the mean squared velocity of fluctuations* [87, 106]. We underline that up to now, besides the BOUSSINESQ assumption (2.1) no other simplifications have been undertaken.

Remark 4. *Despite the fact that we consider a two-dimensional problem, the two-dimensional turbulence is unstable in the sense that a tiny perturbation quickly leads to a fully three-dimensional turbulent state. We would like to underline that equation (2.9) is valid in this case as well. In fact, we can assume that the velocity field* $\boldsymbol{u} = (u, v, \mathrm{w})$ *is such that the mean transverse component* w *is equal identically to zero everywhere, while the averaged fluctuations speed* q *incorporates three components of the velocity field:*

$$q \stackrel{\text{def}}{:=} |\boldsymbol{u}'| \stackrel{\text{def}}{:=} \sqrt{(u')^2 + (v')^2 + (\mathrm{w}')^2}\,.$$

Consequently, we consider a two-dimensional flow embedded into a three-dimensional turbulence state.

In the flow configuration that we consider in the present study, the horizontal momentum is advected vertically by the REYNOLDS stress $\tau = -\rho_0 \overline{u'v'}$. In the developed turbulent flow, the following closure relations have been confirmed experimentally [113]:

$$\overline{u'v'} = -\tilde{\sigma}\, q^2\,, \qquad \tilde{\sigma} \stackrel{\text{def}}{:=} \sigma\, \mathrm{sign}(u_y)\,,$$

where σ is a positive constant which will be considered below as a small parameter. Typically, the value $\sigma \approx 0.15$ corresponds fairly well to the experimental observations. Moreover, the following assumptions are generally adopted [113]:

$$\overline{b'v'} = -\tilde{\sigma}\, q\, \vartheta\,, \qquad \text{where} \qquad \vartheta^2 \stackrel{\text{def}}{:=} \overline{(b')^2}\,.$$

The turbulence is traditionally assumed to be isotropic, *i.e.*

$$\overline{(u')^2} \equiv \overline{(v')^2}\,. \tag{2.10}$$

Finally, the third correlations in Equation (2.9) are supposed to have the following asymptotic behaviour:

$$\overline{\tfrac{1}{2}(u')^3 + \tfrac{1}{2}u'(v')^2 + \frac{p'u'}{\rho_0}} = o(\sigma)\, q^3\,, \qquad \overline{\tfrac{1}{2}(u')^2 v' + \tfrac{1}{2}(v')^3 + \frac{p'v'}{\rho_0}} = o(\sigma)\, q^3\,.$$

Remark 5. *We note that the isotropy condition (2.10) can be relaxed without any change to the subsequent derivation. Namely, we can assume a weaker condition on the averages of quadratic velocity fluctuations:*

$$\overline{(u')^2} \approx \overline{(v')^2}\,,$$

where we allow for small deviations from the isotropy property which can be of the same order than the small parameter σ_0*:*

$$\overline{(u')^2} - \overline{(v')^2} \propto \sigma \cdot q^2\,.$$

*The quantity q should not be confused with the turbulent kinetic energy, which is proportional to q^2 in our notation [87].

Remark 6. *The quantity ϑ represents the magnitude of mean buoyancy fluctuations.*

$$\left(\tfrac{1}{2}\,b^2 \;+\; \tfrac{1}{2}\,\vartheta^2\right)_t \;+\; \left[\left(\tfrac{1}{2}\,b^2 \;+\; \tfrac{1}{2}\,\vartheta^2\right)u\right]_x \;+\; \left[\left(\tfrac{1}{2}\,b^2 \;+\; \tfrac{1}{2}\,\vartheta^2\right)v \;+\; b\,\overline{b'\,v'}\right]_y \;=\; 0\,,$$

where subscripts $_{x,y}$ denote differentiation with respect to those variables. Since the quantity ϑ does not explicitly appear in the final model, we do not include this equation into our consideration. However, this equation is needed, for example, if one is interested in reconstructing the vertical structure of the flow [75, Chapter 7]. This issue will be addressed in future studies.

2.1. Long wave scaling

In order to simplify further the governing equations (2.6) – (2.9) we apply the classical long wave scaling of independent and dependent variables (this operation can be also seen as a passage to thoroughly chosen dimensionless variables):

$$\left\{\begin{array}{llllll} x \;\to\; x\,, & y \;\to\; \varepsilon y\,, & t \to \varepsilon^{-\frac{1}{2}}\,t\,, & \sigma \;\to\; \varepsilon\,\sigma\,, & & \\ u \;\to\; \varepsilon^{\frac{1}{2}}\,u\,, & v \;\to\; \varepsilon^{\frac{3}{2}}\,v\,, & v_s \;\to\; \varepsilon^{\frac{3}{2}}\,v_s\,, & p \;\to\; \varepsilon\,\rho_0\,p\,, & b \;\to\; b\,, & \\ u' \;\to\; \varepsilon^{\frac{1}{2}}\,u'\,, & v' \;\to\; \varepsilon^{\frac{1}{2}}\,v'\,, & p' \;\to\; \varepsilon\rho_0\,p'\,, & b' \;\to\; b'\,, & & \end{array}\right.$$

where $\varepsilon \stackrel{\text{def}}{:=} \left(\frac{h_0}{\ell}\right)^2 \;\ll\; 1$ is the shallowness parameter related to the aspect flow ratio, h_0 being the characteristic flow depth and ℓ the typical wavelength. After applying this rescaling to Equations (2.6) – (2.9) and neglecting the higher order terms in ε we obtain the following system of equations:

$$u_x \;+\; v_y \;=\; 0\,, \tag{2.11}$$

$$b_t \;+\; [\,b\,u\,]_x \;+\; \left[\,b\,(v \;-\; v_s) \;+\; \varepsilon^{-1}\,\overline{b'\,v'}\,\right]_y \;=\; 0\,, \tag{2.12}$$

$$u_t \;+\; \left[\,u^2 \;+\; \mathcal{P}\,\right]_x \;+\; \left[\,u\,v \;+\; \varepsilon^{-1}\,\overline{u'\,v'}\,\right]_y \;=\; 0\,, \tag{2.13}$$

$$\begin{aligned} \left(\tfrac{1}{2}\,(u^2 \;+\; q^2) \;+\; b\,y\right)_t \;+\; \left[\,\tfrac{1}{2}\,(u^2 \;+\; q^2)\,u \;+\; b\,y\,u \;+\; \mathcal{P}\,u\,\right]_x \;+ \\ \left[\,\tfrac{1}{2}\,(u^2+q^2)\,v \;+\; b\,y\,(v \;-\; v_s) \;+\; \mathcal{P}\,v\,\right]_y \;+ \\ \varepsilon^{-1}\,\left[\,u\,\overline{u'\,v'} + y\,\overline{b'\,v'}\,\right]_y \;=\; -\,b\,v_s\,. \end{aligned} \tag{2.14}$$

The pressure $\mathcal{P}$ is defined by the following relations:

$$\mathcal{P}_y \;=\; -b\,, \qquad \mathcal{P} \stackrel{\text{def}}{:=} p \;+\; \overline{(u')^2} \;\equiv\; p \;+\; \overline{(v')^2}\,,$$

where we used the fluctuations isotropy property (2.10). The first relation shows that the pressure $\mathcal{P}$ is hydrostatic. The second relation says that it is not the modified pressure p, which is hydrostatic, but its combination with a component $\overline{(u')^2}$ (or equivalently $\overline{(v')^2}$) of the Reynolds stress. Hereafter we will return to dimensional variables since the long wave scaling was already applied to the governing equations. We mention also that an alternative derivation for a similar depth-averaged system can be found in [62, Appendix A].

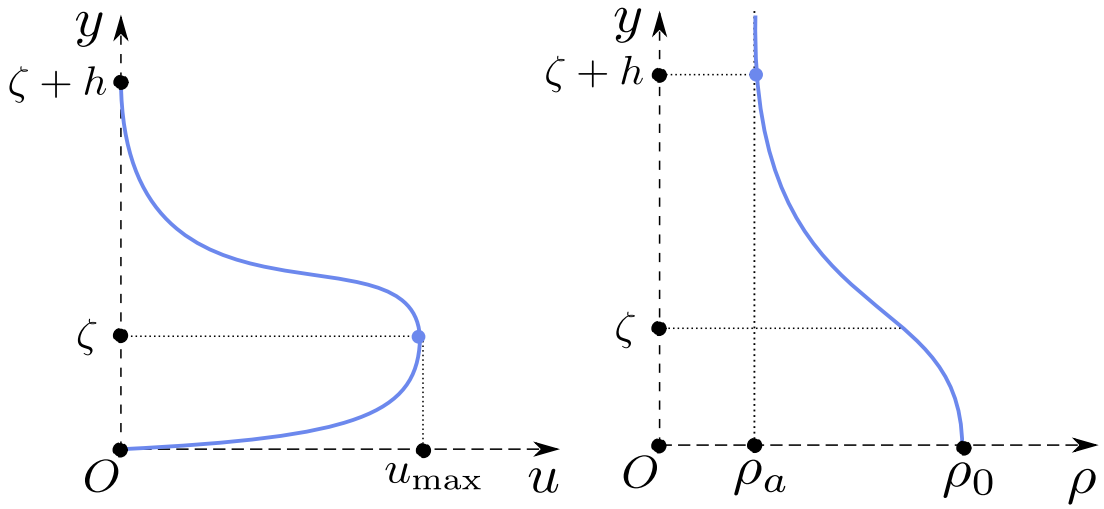

Figure 2. *Vertical flow structure in turbidity currents. On the left image we schematically represent the qualitative behaviour of the horizontal velocity variable u, while on the right image we show the behaviour of the density ρ. The vertical coordinate y is measured from the solid bottom $d(x)$. This schematic representation is supported by findings reported in [100].*

The vertical structure of turbidity gravity flows has been investigated experimentally [1, 45, 100]. The horizontal velocity and density dependence on the flow depth are schematically represented in Figure 2. The density ρ is obviously constant in the bottom (ρ_0) and pure water (ρ_a) layers. In the mixing layer the density varies continuously and almost linearly between two constant boundary values. The horizontal velocity $u(\boldsymbol{x}, t)$ attains its maximum on the boundary between the bottom and mixing layers. Then the velocity $u(\boldsymbol{x}, t)$ goes to zero value on the solid bottom and on the boundary with the still water. The horizontal velocity $u(\boldsymbol{x}, t)$ behaves in the bottom as in a turbulent boundary layer [17, 77, 113]. These experimental evidences suggest us to apply a multi-layer approximation to simplify the model while resolving the vertical structure of the flow.

Consequently, using this a priori knowledge about the flow structure, we will apply the classical vertical averaging operator to obtain a depth-integrated model. We do not provide here the details about these computations, however we recall some basic assumptions we need to adopt:

- The inertial turbulence scale ℓ_t in the mixing layer is determined by large eddies and thus, it is comparable to the layer depth: $\ell_t \propto \zeta$.
- In the upper quiescent layer, by definition, the water is still (without sediment particles) and it is motionless.
- On the solid boundary $y = d(x)$ we have the usual bottom impermeability boundary condition. The Reynolds stresses at the bottom are given by the following relations:

$$\overline{u'v'}\big|_{y=d(x)} \equiv u_*^2 = c_w\, w\,|w| \equiv c_w\, w^2, \qquad w \geqslant 0,$$

Variable	*Significance*
b_s	Buoyancy of sediments
b_0	Buoyancy of the lower (bottom) layer
$b\,(x,\,t)$	Buoyancy in the mixing layer
ζ_s	Thickness of the sediment deposit
$\zeta\,(x,\,t)$	Thickness of the lower (bottom) layer
$h\,(x,\,t)$	Thickness of the mixing layer
$w\,(x,\,t)$	Depth-averaged mean velocity in the bottom layer
$u\,(x,\,t)$	Depth-averaged mean velocity in the mixing layer
$q\,(x,\,t)$	Depth-averaged turbulent kinetic energy in the mixing layer

Table 1. *Definitions of various parameters used in the approximate models. For the illustration see Figure 1. A more complete list of employed nomenclature is given in Appendix C.*

$$\overline{b'v'}\big|_{y\,=\,d\,(x)} \;=\; 0\,.$$

The variable u_* is the so-called friction velocity and the quantity u_*^2 is proportional to the turbulent friction stress* at the solid boundary and $c_w \in \mathbb{R}^+$ is a (positive) constant.

- The sedimentation speed $v_s = 0$ is equal to zero and the buoyancy $b\,(\boldsymbol{x},\,t) \equiv b_0$ is constant in the bottom layer $d\,(x) < y < d\,(x) + \zeta\,(x,\,t)\,.$

The buoyancy b_0 is defined as

$$b_0 \;\stackrel{\text{def}}{:=}\; \frac{(\rho_0 - \rho_a)\,g}{\rho_a}\,. \tag{2.15}$$

The depth-averaged velocities u, w and densities ρ_0, $\bar{\rho}$ are defined in Figure 1 and summarized in Table 1. We reiterate on the fact that the sediments porosity can be taken into account in the present modeling by choosing the sediment concentration $\pi\,(\boldsymbol{x},\,t)$ (appearing in b_0) smaller than one. More complicated approaches exist as well [10, 11, 52, 85, 88, 92].

After performing the depth-averaging operation under the incompressibility condition (2.11) and all the assumptions listed above, we obtain the mass, momentum and energy conservation laws for the averaged quantities:

$$(b_0\,\zeta + b\,h)_t + \left[\,b_0\,\zeta\,w + b\,h\,u\,\right]_x \;=\; 0\,, \tag{2.16}$$

$$(\zeta\,w + h\,u)_t + \left[\,\zeta\,w^2 + h\,u^2 + \tfrac{1}{2}\,b_0\,\zeta^2 + b\,\zeta\,h + \tfrac{1}{2}\,b\,h^2\,\right]_x \\ = -(b_0\,\zeta + b\,h)\,d_x - u_*^2\,, \tag{2.17}$$

*The drag (or friction) associated with bottom must be parametrized since shallow water depth-averaged equations do not resolve turbulence produced at this boundary. This is commonly achieved by introducing a drag coefficient along with an empirical law for the shear velocity near the bottom.

$$\begin{aligned}\left(\zeta\, w^2 \;+\; h\,(u^2+q^2) \;+\; b_0\,\zeta^2 \;+\; 2\,b\,\zeta\,h \;+\; b\,h^2\right)_t \;+\\ \left[\zeta\, w^3 \;+\; h\,u\,(u^2+q^2) \;+\; 2\,b_0\,\zeta^2\,w \;+\; 2\,b\,\zeta\,h\,w \;+\; 2\,b\,(\zeta+h)\,h\,u\right]_x \;=\\ -\,\mathcal{E} \;-\; 2\,(b_0\,\zeta\,w \;+\; b\,h\,u)\,d_x\,, \qquad (2.18)\end{aligned}$$

where we introduce into the model a dissipative term $\mathcal{E}$ coming from the turbulent energy dissipation [73, 109]. The form of this dissipative term has to be specified. The bottom stress (or friction) term τ_* was already specified above. We remind that in the high REYNOLDS number regime, the following expression is widely used:

$$u_*^2 \;=\; c_w\, w^2\,.$$

For the sediments layer we can write a separate momentum balance equation after the same averaging procedure:

$$w_t \;+\; \left[\tfrac{1}{2}\,w^2 \;+\; b_0\,\zeta \;+\; b\,h\right]_x \;=\; -b_0\,d_x \;-\; \frac{u_*^2}{\zeta}\,, \qquad (2.19)$$

provided that the layer height $\zeta \;>\; 0$. These equations have to be completed by two kinematic conditions on the interfaces:

$$\zeta_t \;+\; [\,\zeta\, w\,]_x \;=\; \chi^-\,, \qquad (2.20)$$

$$h_t \;+\; [\,h\,u\,]_x \;=\; \chi^+\,, \qquad (2.21)$$

where the terms $\chi^\pm$ are the entrainment rates which account for the mass exchanges between the layers. The mass exchange between the mixing and ambient layers is driven by the widely known KELVIN–HELMHOLTZ instability [55]. This suggests also the presence of an underlying coupled hydrodynamic/sediment layer instability as well.

Using Equations (2.19), (2.20) and (2.21) the just derived conservation laws (2.16) – (2.18) can be rewritten also in the following non-conservative form (the whole system is listed here):

$$\zeta_t \;+\; [\,\zeta\, w\,]_x \;=\chi^-\,, \qquad (2.22)$$

$$h_t \;+\; [\,h\,u\,]_x \;=\chi^+\,, \qquad (2.23)$$

$$w_t \;+\; w\,w_x \;+\; [\,b_0\,\zeta \;+\; b\,h\,]_x \;=\; -\,b_0\,d_x \;-\; \frac{u_*^2}{\zeta} \qquad (2.24)$$

$$b_t \;+\; u\,b_x \;=\; -\,\frac{b_0\,\chi^- \;+\; b\,\chi^+}{h}\,, \qquad (2.25)$$

$$u_t \;+u\,u_x \;+\; b\,[\,\zeta+h\,]_x \;+\; \tfrac{1}{2}\,h\,b_x \;=\; -\,\frac{w\,\chi^- \;+\; u\,\chi^+}{h} - b\,d_x\,, \qquad (2.26)$$

$$\begin{aligned}q_t \;+\; u\,q_x \;&=(2\,h\,q)^{-1}\Big[\left(2\,w\,u \;-\; w^2 \;+\; b_0\,h \;-\; 2\,b\,h\right)\chi^- \;+\\ &\left(u^2 \;-\; q^2 \;-\; b\,h\right)\chi^+ \;-\; \mathcal{E} \;-\; b\,h\,v_s\Big]\,. \qquad (2.27)\end{aligned}$$

In particular, this computation shows that our system possesses multiple contact characteristics $\dfrac{\mathrm{d}x}{\mathrm{d}t} \;=\; \xi_{3,\,4} \;=\; u$ (the indices 3 and 4 will become clearer below in Section 2.4). Below we will use this property to extract from this model a subsystem which governs the

mixing layer dynamics. At the current stage, disregarding the particular form of the mixing terms, our model has the structure of a two-layer shallow water system coupled with two advection equations: one for the buoyancy and another one describes the transport of the turbulent averaged velocity fluctuations. In order to close the system above, we have to specify the entrainment rates $\chi^{\pm}$ among fluid layers and the energy dissipation term $\mathcal{E}$. Some approaches to determine entrainment rates are explained below. For the dissipative term, we assume the following closure relation:

$$\mathcal{E} \stackrel{\text{def}}{:=} \kappa q^3, \qquad \text{where} \qquad \kappa > 0.$$

2.2. Determination of entrainment rates without sedimentation

If the sedimentation velocity $v_s \equiv 0$, the main hypothesis that we can make about the entrainment rates $\chi^{\pm}$ is that they are related to the mean square root of the turbulent velocity q. The simplest dependence is the linear proportionality and we adopt it in our study:

$$\chi^{\pm} \propto \sigma^{\pm} q. \tag{2.28}$$

Depending on the flow type, which is realized in practice, the closure law (2.28) can be further refined. For instance, we may distinguish between two following situations:

- The mass transfer takes place at upper and lower boundaries of the turbulent layer (the so-called "mixing layer" described below in Section 3.1)
- The mass transfer takes place only at the upper boundary (the so-called bottom turbulent jet)

So, a more accurate closure relation for mixing layers is obtained by taking $\sigma^+ \equiv 2\sigma$, $\sigma^- \equiv -\sigma$, yielding the following expressions for entrainment rates:

$$\chi^+ = 2\sigma q, \qquad \chi^- = -\sigma q. \tag{2.29}$$

For bottom turbulent jets we propose the following closure $\sigma^+ \equiv \sigma$, $\sigma^- \equiv 0$, which yields

$$\chi^+ = \sigma q, \qquad \chi^- = 0. \tag{2.30}$$

The constant σ is usually taken to be $\sigma \approx 0.15 \sim 0.17$ and they characterizes the ratio of the characteristic vertical to horizontal flow scales in the long wave approximation. In the case of flat bottom without friction, the constant σ can be completely removed from equations by a suitable scaling of independent variables. We introduce also a new constant δ as the ratio of two previously introduced constants:

$$\delta \stackrel{\text{def}}{:=} \frac{\kappa}{\sigma} > 0. \tag{2.31}$$

This constant δ shall be used in developments below. In practice, δ is taken in the range

$$0 \leqslant \delta \lesssim 8.0.$$

We observed using numerical means that δ has a weak influence on the qualitative properties of unsteady simulations. We would like to mention also that a number of authors considered

simple constant entrainment rate coefficients independent of RICHARDSON number [15, 105, 111, 116].

2.3. Determination of entrainment rates with sedimentation

In order to prescribe the expressions for $\chi^{\pm}$ in terms of other physical quantities, we analyze an idealized situation schematically depicted in Figure 3. Namely, we consider a flat bottom, the horizontal motion is absent and the flow is invariant under the horizontal translations. In other words, we study the evolution of this layered system under the sedimentation dynamics with a constant fall speed v_s. We denote by $y(t)$ the supposed upper boundary of particles which will become a part of the sediment layer at the next time moment $t + \Delta t$. The upper boundary $h(t)$ will fall with the speed v_s, while the lower layer will grow with some velocity v_b which is yet to be determined. By definition, the entrainment rates $\chi^{\pm}$ can be expressed in terms of v_s and v_b as follows:

$$\chi^{+} \stackrel{\text{def}}{:=} v_s - v_b, \qquad \chi^{-} \stackrel{\text{def}}{:=} v_b.$$

In order to determine the speed v_b we will write two kinematic conditions and one sediments mass conservation equation:

$$\begin{aligned} \zeta(t + \Delta t) - \zeta(t) &= v_b \cdot \Delta t, \\ y(t) - \zeta(t + \Delta t) &= v_s \cdot \Delta t, \\ \big(\zeta(t + \Delta t) - \zeta(t)\big)\,\pi^{-}\rho_0 &= \big(y(t) - \zeta(t)\big)\,\pi^{+}\rho. \end{aligned}$$

By solving these relations, one can easily find the following expression for the sediments layer growth velocity v_b:

$$v_b \equiv \frac{v_s \cdot \pi^{+}}{\pi^{-} - \pi^{+}}.$$

Finally, in the presence of the turbulent flow we complete the just derived expression of χ^{+} by a term σq responsible of the still water entrainment into the mixing layer. Thus, the final expressions are

$$\chi^{-} = \frac{v_s \cdot b}{b_0 - b} \equiv v_b, \qquad \chi^{+} = -\frac{v_s \cdot b_0}{b_0 - b} + \sigma q, \tag{2.32}$$

where we replaced equivalently the volume fractions $\pi^{\pm}$ by buoyancy variables b_0, b, since the system is written using these variables. As one can see, in the mixing layer we have two competing effects: the sedimentation of particles down to the bottom and the pure water entrainment into the mixing layer.

2.3.1 Simplified model

Entrainment rates closure (2.32) can be further simplified if we notice that the density of entrained sediments is much lower than sediments layer in the vicinity of the solid bottom.

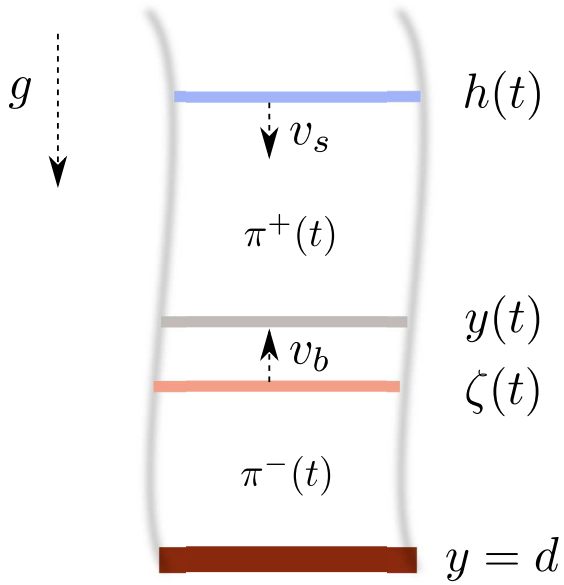

Figure 3. *Schematic illustration to the sedimentation process of a uniform layer in the horizontal extent.*

In other words, we can assume that $b \ll b_0$. Under this assumption Equation (2.32) becomes

$$\chi^- \equiv 0, \qquad \chi^+ = \sigma q - v_s. \tag{2.33}$$

The main difference with the closure proposed in Section 2.2 is that χ^- vanishes and χ^+ takes into account the sedimentation velocity v_s. Notice also that the sedimentation velocity v_s can take eventually zero value and in this way we recover the previously proposed closure relation (2.30). This situation is not excluded. This closure turns out to be useful if we aim mostly to describe the dynamics of the mixing layer and of bottom buoyancy jets. In particular, it will be successfully used to explain some experiments from [103].

2.3.2 Intermediate conclusions

Let us summarize the developments made so far. The proposed model is self-consistent and depends essentially on the values of three constants σ, δ and c_w, which are to be specified before the simulations can be run. Our model covers also the situation where the intermediate mixing layer reaches the bottom and transforms into the so-called bottom buoyancy jet. It happens when $\zeta \ll h$. In this case one has to set $\chi^- = 0$ and the computations can be continued. We are aware of the fact that the mixing layer cannot "touch" the bottom *stricto sensu*. There is always a little layer of a heavy fluid with density close to ρ_0. However, this layer* is dynamically passive since the gravity and bottom friction forces are in equilibrium. In situations, where the mixing layer does not

*It is depicted in Figure 1 under the dense current and it has the velocity $w(x, t)$ along with the thickness $\zeta(x, t)$.

approach bottom (yet), this tiny layer plays the rôle in alimenting the flow head with new sediment particles. Moreover, the flow head can be supplied by sediments of density ρ_0 located immediately after the front in the downstream direction since the mixing process is most significant close to the front of the gravity current. Some mathematical considerations on this situation are given in the following Section.

2.4. Sediments equilibrium model

Hereafter we consider a special regime where the flow attains the equilibrium state in the lowest bottom layer. Namely, we assume that the gravity force balances exactly the turbulent friction at the solid bottom, *i.e.*

$$\frac{c_w\, w^2}{\zeta} \;\equiv\; -b_0\, d_x\,. \tag{2.34}$$

In other words, the right-hand side of equation (2.19) vanishes and this relation provides us an expression of the velocity w as a function of the bottom layer thickness ζ and of the local bottom slope d_x :

$$w \;\equiv\; \psi(\zeta,\, x) \;\stackrel{\text{def}}{:=}\; \sqrt{-\frac{b_0\,\zeta\, d_x}{c_w}}\,, \qquad d_x \;\leqslant\; 0\,,$$

where we choose the positive branch of solutions $w \;>\; 0$, since the flow is expected to move downwards. The bottom layer thickness can be determined by solving the corresponding kinematic condition (2.20):

$$\zeta_t \;+\; \big[\,\zeta\cdot\psi(\zeta,\, x)\,\big]_x \;=\; \chi^-\,. \tag{2.35}$$

The last equation is related to the rest of the system only through the entrainment rate χ^- at the right-hand side. Thus, the rest of the *equilibrium* system reads:

$$h_t \;+\; [\,h\,u\,]_x \;=\; \chi^+\,, \tag{2.36}$$

$$u_t \;+\; u\,u_x \;+\; b\,h_x \;+\; \tfrac{1}{2}\,h\,b_x \;=\; -b\,d_x \;-\; b_0\,\zeta_x \;-\; \frac{\psi\,\chi^- \;+\; u\,\chi^+}{h}\,, \tag{2.37}$$

$$b_t \;+\; u\,b_x \;=\; -\,\frac{b_0\,\chi^- \;+\; b\,\chi^+}{h}\,, \tag{2.38}$$

$$q_t \;+\; u\,q_x \;=\; (2\,q\,h)^{-1}\,\big[\,(2\,\psi\,u \;-\; \psi^2 \;+\; b_0\,h \;-\; 2\,b\,h)\,\chi^- \tag{2.39}$$

$$+\; (u^2 \;-\; q^2 \;-\; b\,h)\,\chi^+ \;-\; \kappa\,q^3 \;-\; b\,h\,v_s\,\big]\,. \tag{2.40}$$

The last system is always hyperbolic* with characteristic speeds $\left\{ \xi_i \right\}_{i=1}^{5}$ which can be easily computed:

$$\begin{aligned} \frac{\mathrm{d}x}{\mathrm{d}t} &= \xi_{1,2} = u \pm \sqrt{b\,h}\,, \\ \frac{\mathrm{d}x}{\mathrm{d}t} &= \xi_{3,4} = u\,, \\ \frac{\mathrm{d}x}{\mathrm{d}t} &= \xi_5 = \psi + \frac{\partial \psi}{\partial \zeta}\,\zeta\,. \end{aligned}$$

The last characteristic ξ_5 corresponds to kinematic waves in the lowest bottom layer described by Equation (2.35).

2.5. Equilibrium model without sedimentation

The system derived in the previous Section can be further simplified if we neglect the effect of the sedimentation velocity v_s. In other words, hereafter we will set this parameter to zero:

$$v_s \equiv 0\,. \tag{2.41}$$

This approximation is valid in a fully developed turbulent flow on time scales comparable to the lifetime of large structures (the so-called inertial range). It can be also seen from a different physical perspective: the sedimentation can be neglected while the transport of sediment particles is governed by the main eddies of the gravity current over an incline. Of course, it has to be taken into account in regions where the suspension particles trajectory looks like a free fall. Under the assumption (2.41), the entrainment rates $\chi^{\pm}$ according to (2.33) become

$$\chi^{-} \equiv 0\,, \qquad \chi^{+} \equiv \sigma\, q\,,$$

which implies that the kinematic equation (2.35) is completely decoupled from System (2.36) – (2.40). The information about ζ is transported along characteristics of this equation with the speed ξ_5. So, if ζ is constant initially and this constant value is maintained at the channel inflow, ζ will remain so under the system dynamics. We will adopt this assumption as well in order to focus our attention on the mixing layer dynamics. Below we will consider only the middle mixing layer. Under these conditions, the equilibrium model (2.36) – (2.40)

*In order to check it one has to write it in conservative variables, compute the Jacobian matrix of the advective flux with respect to conservative variables and find its eigenvalues [72]. We skip these standard steps for the sake of brevity of this study.

becomes:

$$h_t + [h\,u]_x = \sigma\,q\,, \tag{2.42}$$

$$b_t + u\,b_x = -\frac{\sigma\,q\,b}{h}\,, \tag{2.43}$$

$$u_t + u\,u_x + b\,h_x + \tfrac{1}{2}\,h\,b_x = -\frac{\sigma\,q\,u}{h} - b\,d_x\,, \tag{2.44}$$

$$q_t + u\,q_x = \sigma\,\frac{u^2 - q^2 - h\,b - \delta q^2}{2h}\,, \tag{2.45}$$

where the constant δ was defined above in (2.31). The system (2.42) – (2.45) can be equivalently recast in the conservative form which has an advantage to be valid for discontinuous solutions as well [47, 72]:

$$h_t + [h\,u]_x = \sigma\,q\,, \tag{2.46}$$

$$(h\,b)_t + [h\,b\,u]_x = 0\,, \tag{2.47}$$

$$(h\,u)_t + \left[h\,u^2 + \tfrac{1}{2}\,b\,h^2\right]_x = -h\,b\,d_x\,, \tag{2.48}$$

$$\left(h\,(u^2 + q^2 + h\,b)\right)_t + \left[(u^2 + q^2 + 2\,h\,b)\,h\,u\right]_x = -2\,h\,b\,u\,d_x - \kappa\,q^3\,. \tag{2.49}$$

Here, $\kappa \in \mathbb{R}^+$ is a positive constant measuring the rate of turbulent dissipation [73, 109].

An important property of this model is the absence of the bottom friction term. This physical effect was taken into account in (2.34) while excluding the bottom layer (of thickness $\zeta(x,\,t)$). This gives us the mathematical reason for the absence of a friction term in model (2.46) – (2.49). Similarly, we can bring also a physical argument to support this fact. The horizontal velocity takes the maximum value on the boundary between the bottom sediment and mixing layers (see Figure 2). Consequently, the REYNOLDS stress τ_* vanishes here.

Remark 7. *In fact, we can derive an additional balance law by combining together equations* (2.42) *and* (2.45)*:*

$$(h\,q)_t + [h\,q\,u]_x = \tfrac{1}{2}\,\sigma\,\left(u^2 + (1-\delta)\,q^2 - h\,b\right).$$

The last equation is not independent from equations (2.46) – (2.49)*. Consequently, it does not bring new information about the equilibrium sedimentation-free model* (2.42) – (2.45)*. Nevertheless, we provide it here for the sake of the exposition completeness.*

The proposed model has an advantage of being simple, almost physically self-consistent* and having the hyperbolic structure. It was derived for the first time in [75, Chapter 5]. In order to obtain a well-posed problem the system (2.46) – (2.49) has to be completed by corresponding boundary and initial conditions. In the following sections, the just derived equilibrium system (2.46) – (2.49) will be studied in more details by analytical and numerical means.

*Only two constants σ and δ need to be prescribed to close the system.

3. Analytical study of the model

In this Section we discuss the steady state solutions and investigate the qualitative behaviour of two important special classes of solutions — travelling waves and similarity solutions.

3.1. Mixing layer formation

Mixing layers are formed between two fluid layers having different densities. The initial stages of mixing processes play a very important rôle in natural and laboratory environments. The physical mechanism of a mixing layer formation is given by various interfacial instabilities (*e.g.* Rayleigh–Taylor or Kelvin–Helmholtz). The most important mechanism is, of course, the Kelvin–Helmholtz instability [55] because of the shear velocity presence [100]. In supercritical flows the mixing intensity is considerably intensified. In this way, mixing layers are the most pronounced in transcritical flows over underwater obstacles (*i.e.* bathymetric features), since a jet is formed on the obstacle downstream (lee) side making the flow supercritical. The process of mixing layer formation over an inclined bottom was studied in [74] in the framework of a three-layer model. In the present study we apply a similar approach to the two-layer* System (2.22) – (2.27). Below we derive a steady solution, which provides the boundary conditions for the unsteady propagation of the flow head (see Figure 1).

Stationary solutions to System (2.22) – (2.27) satisfy the following system of differential equations:

$$
\begin{aligned}
w\,\zeta_x \;+\; \zeta\,w_x \;&=\; \chi^-\,,\\
u\,h_x \;+\; h\,u_x \;&=\; \chi^+\,,\\
w\,w_x \;+\; b_0\,\zeta_x \;+\; b\,h_x \;+\; h\,b_x \;&=\; -b_0\,d_x \;-\; \frac{\tau_*}{\zeta}\,,\\
u\,u_x \;+\; b\,(\zeta_x \;+\; h_x) \;+\; \tfrac{1}{2}\,h\,b_x \;&=\; -\,b\,d_x \;-\; \frac{w\,\chi^- \;+\; u\,\chi^+}{h}\,,\\
h\,u\,b_x \;&=\; -b_0\,\chi^- \;-\; b\,\chi^+\,,\\
2\,q\,h\,u\,q_x \;&=\; \bigl(2\,w\,u \;-\; w^2 \;+\; b_0\,h \;-\; 2\,b\,h\bigr)\,\chi^-\\
&\quad+\; \bigl(u^2 \;-\; q^2 \;-\; b\,h\bigr)\,\chi^+ \;-\; \kappa\,q^3\,.
\end{aligned}
$$

The last system of equations can be seen as a quasilinear system with respect to spatial derivatives of unknown variables $\bigl(h_x,\,u_x,\,b_x,\,\zeta_x,\,w_x,\,q_x\bigr)$. The determinant $\Delta\,(x)$ of this system is

$$
\Delta\,(x) \;=\; \bigl(u^2 \;-\; b\,h\bigr)\cdot\bigl(w^2 \;-\; b_0\,\zeta\bigr) \;-\; b^2\,\zeta\,h\,. \tag{3.1}
$$

*We remind that the upper layer of the still water is assumed to be motionless in the present study.

By assuming that $\Delta \neq 0$, we obtain:

$$h_x = \frac{a_1 \cdot b h + a_2 \cdot \left(w^2 - b_0 \zeta\right)}{\Delta}, \tag{3.2}$$

$$u_x = \frac{\chi^+ - u h_x}{h}, \quad (h_x \text{ should be taken from the previous equation}) \tag{3.3}$$

$$b_x = -\frac{b_0 \chi^- + b \chi^+}{h u}, \tag{3.4}$$

$$\zeta_x = -\frac{1}{b}\left(\tfrac{1}{2} h b_x + \frac{w \chi^- + u \chi^+}{h} + u u_x\right) - h_x - d_x, \tag{3.5}$$

$$w_x = \frac{\chi^- - w \zeta_x}{\zeta}, \tag{3.6}$$

$$q_x = \frac{\left(2 w u - w^2 + b_0 h - 2 b h\right) \chi^- + \left(u^2 - q^2 - b h\right) \chi^+ - \kappa q^3}{2 q h u}, \tag{3.7}$$

where the coefficients $a_{1,2}$ are defined as

$$a_1 \stackrel{\text{def}}{:=} \chi^- w + b_0 \zeta d_x + \tau_*,$$
$$a_2 \stackrel{\text{def}}{:=} \chi^+ u + b h d_x + w \chi^- + u \chi^+.$$

The last system of equations can be seen as an Initial Value Problem (IVP) in the spatial variable x, if all spatial derivatives in the right-hand side are replaced by their expressions (we do not make this operation to keep the shorthand notation). We illustrate below the behaviour of solutions to System (3.2) – (3.7) on the example of the mixing layer formation problem over an inclined bottom. The real data to build this solution were taken from [101].

3.1.1 Problem statement and solution

In this Section we formulate the IVP inspired by the experimental study [101]. Consider a density current over the flat plane inclined with angle φ with respect to the horizontal direction. Without any loss of generality, we postulate that the mixing layer starts to form at some location $x = x_0$, where we set the initial conditions for the steady System (3.2) – (3.7). Moreover, we adopt the closure (2.29). We assume that in this point we have a supercritical flow with velocity w_0, height ζ_0 and density ρ_0. The upper layer of still water with density ρ_a is motionless. Thus, we have

$$w_0^2 > b_0 \zeta_0,$$

and b_0 was defined earlier in (2.15). The initial height of the mixing layer is $h_0 = 0$ by our assumption on point x_0. The initial asymptotic stages of the mixing layer formation as $x \to x_0$ can be determined from the condition that the right hand sides in (3.2) – (3.7) are bounded [74, 75]:

$$b_L = \tfrac{1}{2} b_0, \qquad u_L = \tfrac{1}{2} w_0, \qquad q_L = \frac{w_0}{\sqrt{4 + 2\delta}}.$$

Under the condition $\zeta > 0$, we shall have $b(x) \equiv b_L = \frac{1}{2} b_0$. This can be seen after substituting the closure relations for $\chi^{\pm}$ from Equation (2.29) into Equation (3.4). One readily obtains that

$$b_x = -\frac{\sigma q (b_0 - 2b)}{h u}.$$

From the the condition $b_L = \frac{1}{2} b_0$, it follows that $b(x) \equiv \frac{1}{2} b_0$.

By taking into account the last asymptotics for the solution, we can construct it using standard numerical means until the point x_1, where the mixing layer will touch the bottom, *i.e.* the point where $\zeta(x_1) \equiv 0$. The solution to system (3.2) – (3.7) taking into account the aforementioned asymptotics is depicted in Figure 4. We used the following set of physical parameters in our computations:

$$\sigma = 0.15, \qquad \delta = 6, \qquad \varphi = 10.8^\circ, \qquad x_0 = 8\,\mathsf{cm},$$
$$\zeta_0 = 7\,\mathsf{cm}, \qquad w_0 = 5\,\frac{\mathsf{cm}}{\mathsf{s}}, \qquad b_0 = 1.4\,\frac{\mathsf{cm}}{\mathsf{s}^2}.$$

The flow geometry along with the initial conditions were taken from [101]. On the upper panel of Figure 4 we show the comparison with experimental data provided by Armi & Pawlak (2000) [101], who employed the Laser Induced Fluorescence (LIF) and Digital Particle Imaging Velocimetry (DPIV) together with a concentration of rhodamine dye for flow visualization. Color code corresponds to the density gradient (blue is lower, red is higher). Their results show that instabilities evolve in an asymmetrical manner. In Figure 4 with a dashed line we show the numerical prediction given by function $y = \zeta(x)$ (lower line) and $y = \zeta(x) + h(x)$ (upper line). The reasonable agreement between the experimental data and our numerical solution at the initial parts of the mixing layer validate the approximate model (at least for steady solutions). We would like to mention that in the experiment (as well as in the nature), there is a slight backward flow above the mixing layer. The typical velocities are of the order $0.5 \sim 1\ \frac{\mathsf{cm}}{\mathsf{s}}$. In our model this effect is not taken into account. It could be done by including the third (upper) layer into consideration [74]. On the left and right sub-plots in upper Figure 4, we show the experimental distribution of the velocity (solid line) and of the density (dashed line) at the beginning and at the end of the considered fluid domain.

The theoretical lower bound of the mixing layer coincides fairly well with the experimental estimation of the high density gradient area as it can be seen in Figure 4 (upper panel). On the other hand, the theoretical upper bound goes sufficiently higher than the coloured region measured experimentally. This little discrepancy comes from the fact that the experimental data report the high density gradient, while our model predicts the upper bound of large vortices appearing during nonlinear stages of the Kelvin–Helmholtz (KH) instability development [55]. This situation is described in more details in [75, Chapter 7, § 3]. The experimental evidence for the KH mechanism is shown in [101, Figure 8]. In particular, it is shown there that the mixing layer growth into the still water is

$$\frac{\mathrm{d}h}{\mathrm{d}x} = 2\sigma \equiv 0.3 \quad \text{(in our computation)}.$$

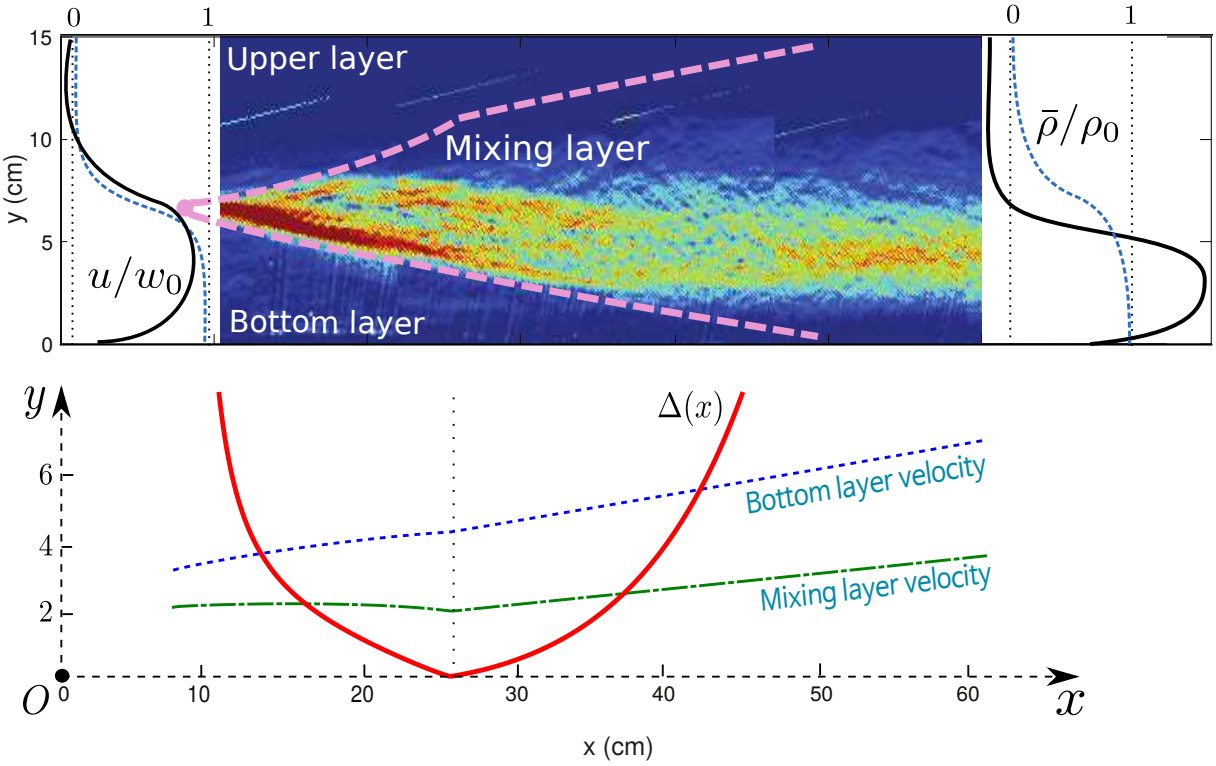

Figure 4. *The density gradient field image: comparison with the experimental measurements using Laser Induced Fluorescence (LIF) [101]. The picture is rotated so that the slope becomes horizontal.*

In the same time, the effective thickness of the mixing layer grows according the computed velocity profile as

$$\frac{\mathrm{d}h_{\mathrm{eff}}}{\mathrm{d}x} \approx 0.18\,.$$

This value corresponds much better to numerous experimental findings [75, Fig. 7.4]. Consequently, we may conclude that in the considered case of the stratified fluid flow down the incline, the *effective* height* of the mixing layer will be smaller than the height of the computed turbulent layer.

In Figure 4(lower panel) we show with dotted lines the (theoretically predicted) distribution of velocities $u\,(x)$ and $w\,(x)$ in the mixing layer. The slope rupture in these curves is visible. It happens since at $x_c \approx 26$ cm the determinant (3.1) vanishes, *i.e.*

$$\Delta\,(x_c) \equiv 0\,.$$

Physically speaking it means that the flow remains everywhere supercritical. However, for small changes of the flow parameters, it is possible that hydraulic jumps will appear along with following local subcritical zones. We note also that internal hydraulic jumps on the

*We remind here the definition of the effective height of the mixing layer: it is the fluid body bounded from above and below by virtual surfaces where $w = 0.95 \times w_0$ and $w = 0.1 \times w_0$ correspondingly. The asymmetry in this definition comes from the nonlinear form of the vertical velocity profile.

downstream side of an underwater obstacle is an important feature of stratified flows (both in the ocean and in the atmosphere). The inclusion of the mixing layer formation before the hydraulic jump is of capital importance in such situations.

3.1.2 Sediment layer

When the mixing layer approaches the lower boundary with sediment deposits, the mass entrainment from the lowest layer decelerates and stops completely. In the framework of our model, this effect could be realized by ensuring the transition from $\chi^- = -\sigma\, q$ towards $\chi^- = 0$ (and, correspondingly, from $\chi^+ = 2\,\sigma\, q$ towards $\chi^+ = \sigma\, q$). Physically it means that that the maximum of the flow velocity is achieved somewhere near the boundary between the mixing layer and bottom layer of constant density ρ_0. The transition to $\chi^- = 0$ takes place in neighbourhood of the right boundary of the flow represented in Figure 4.

3.1.3 Intermediate conclusions

The mixing layer structure over a downhill determines the flow structure further down. In particular, the total mass flux (relative to fluid density ρ_a) $\mathcal{M}_0 = b_0\,\zeta_0\,w_0$ is divided into two parts. Namely, this splitting takes place at the point of transition of the mixing layer into the turbulent jet and the undiluted bottom layer, *i.e.* at $x = x_1$.

The turbulent jet receives the buoyancy flux $\mathcal{M}_j = b_1\,h_1\,u_1$, while the bottom layer takes $\mathcal{M}_b = b_0\,\zeta_1\,w_1$. We notice also that for the slope angle $\varphi = 10.8^\circ$ and experimental facilities considered in Figure 4, the dominant part of the mass flow goes into the turbulent jet, *i.e.* $\mathcal{M}_j \gg \mathcal{M}_b$.

If we assume that the flow velocity at $x = x_1$ in the bottom layer stabilizes* due to small thickness of the layer, in the bottom layer we have $w \equiv w_b$, $\zeta \equiv \zeta_b$ and the density in the layer does not change anymore. Hence, the bottom layer becomes completely passive in the flow dynamics. But in the same time it influences the flow head propagation velocity for moderate bottom slopes†. This point will be demonstrated below.

3.2. Steady flows

From numerical and experimental points of view, a significant amount of work has been devoted to the study the transient gravity current problem. The steady flow configuration has received less attention. However, when one has a dynamical system in hands, it is natural to begin its study by looking for equilibrium points [63]. Thus, the study of a mathematical model is not complete if we do not discuss this class of solutions. Moreover,

*Physically it happens when the gravity force projection along the slope is balanced by the friction force with the rigid bottom.

†For large inclines the physical mechanisms are slightly different.

stationary solutions may be *realized* and *observed* on certain time scales in laboratory experiments, if certain conditions are met and maintained during sufficiently long time. For instance, the buoyant flow entering the inclined channel has to be maintained at constant rate during the whole experiment. If permanent boundary conditions are maintained not only in the mixing layer, but also in the bottom layer as well, then, the lower sediment layer will play a passive rôle in the flow, *i.e.*

$$\zeta_b \;=\; \text{const}\,, \qquad w_b \;=\; \text{const}\,, \qquad \rho_0 \;=\; \text{const}\,.$$

In other words, the friction and mixing between these two layers do not take place. It is not difficult to see that fluid flows of the form

$$u \;\equiv\; u_j\,, \qquad m \;=\; b\,h \;\equiv\; m_j\,, \qquad q \;\equiv\; q_j$$

satisfy Equations (2.42) – (2.45) provided that the mixing layer thickness depends linearly on the coordinate x along the channel, *i.e.*

$$h\,(x) \;=\; h_0 \;+\; \varsigma\cdot(x \;-\; x_0)\,.$$

Here, quantities with sub-script j denote values in the steady jet. The variable m will be sometimes referred as the mass, however, physically it represents the excess of the fluid column weight with respect to the still water level due to the presence of heavy sediment suspensions. To satisfy the system (2.42) – (2.45), the following identities have to be satisfied:

$$\varsigma\cdot u_j \;=\; \sigma\cdot q_j\,, \tag{3.8}$$

$$\varsigma\cdot\left(u_j^2 \;+\; \tfrac{1}{2}\,m_j\right) \;=\; \alpha\cdot m_j\,, \tag{3.9}$$

$$\varsigma\cdot\left(u_j^2 \;+\; q_j^2 \;+\; 2\,m_j\right)\cdot u_j \;=\; 2\,\alpha\cdot m_j\cdot u_j \;-\; \kappa\,q_j^3\,, \tag{3.10}$$

where $\alpha \overset{\text{def}}{:=} -\,d_x \;\geqslant\; 0$. An algebraic consequence of the first two relations (3.8) – (3.9) above can be easily derived:

$$u_j^2 \;-\; m_j \;-\; (1 \;+\; \delta)\,q_j^2 \;=\; 0\,.$$

The boundary conditions specify also the buoyancy influx $\mathcal{M}_j$ into the channel:

$$\mathcal{M}_j \;\overset{\text{def}}{:=}\; m_j\cdot u_j \;=\; U_j^3 \qquad\Longrightarrow\qquad U_j \;=\; \sqrt[3]{\mathcal{M}_j}\,.$$

All the relations above can be combined into a single equation for the quantity $\mathcal{A}_j \overset{\text{def}}{:=} \dfrac{u_j}{U_j}$ using simple algebraic transformations (see also Appendix A.1):

$$\sqrt{\frac{1 \;-\; \mathcal{A}_j^{-3}}{1 \;+\; \delta}}\,\left(1 \;+\; 2\,\mathcal{A}_j^3\right) \;=\; \frac{2\,\alpha}{\sigma}\,.$$

There exists a unique solution to this equation for any positive right hand side. Moreover, it can be shown that $\mathcal{A}_j \;>\; 1$. It corresponds to the supercritical flow with $u_j^2 \;>\; m_j$. Then, once we determined $\mathcal{A}_j$, from Equations (3.8) – (3.10) we can determine the remaining quantities u_j, m_j, q_j and ς.

To make a conclusion, in turbidity gravity flows in an inclined channel, where the horizontal (depth-integrated) velocity maximum is achieved on the boundary between the sediment and turbulent mixing layers, the model (2.42) – (2.45) predicts the stationary *supercritical* flow with pure fluid entrainment from the upper layer.

3.3. Travelling waves

One of the main questions in the modelling of turbidity flows is to determine the density front velocity. The proposed base model (2.42) – (2.45) is sufficiently simple to address this question analytically.

3.3.1 General considerations

In this Section we describe the class of travelling wave solutions to System (2.46) – (2.49) in their generality. Since we are mainly interested in smooth solutions, we will use the characteristic form (2.42) – (2.45) for the sake of convenience. Also, we assume that the bottom slope α is constant, which is necessary for the existence of solutions with permanent shape.

The travelling wave ansatz takes the following form:

$$h(x,t) = h(\xi), \quad m(x,t) = m(\xi), \quad u(x,t) = u(\xi), \quad q(x,t) = q(\xi),$$

where $\xi \stackrel{\text{def}}{:=} x - c\cdot t$ and c is a positive* constant, which has the physical sense of the travelling wave speed (to be determined later). After substituting this ansatz into Equations (2.42) – (2.45), we obtain a system of Ordinary Differential Equations (ODEs):

$$(u-c)\,h' + hu' = \sigma\, q\,, \tag{3.11}$$

$$(u-c)\,m' + m\,u' = 0\,, \tag{3.12}$$

$$(u-c)\,u' + \frac{1}{2}\,m' + \frac{m}{2h}\,h' = \frac{\alpha m - \sigma\, q\, u}{h}\,, \tag{3.13}$$

$$(u-c)\,q' = \frac{\sigma\big(u^2 - (1+\delta)q^2 - m\big)}{2\,h}\,, \tag{3.14}$$

where the prime $'$ denotes the differentiation operation with respect to ξ. This system of ODEs describes a transcritical gravity flow in a coordinate system which moves with velocity c. More precisely, the flow is of supercritical type in the avalanche core and it switches to the subcritical regime when we cross the wave front. By analogy with the detonation theory [41], the front velocity c (under certain conditions) is given by the Chapman–Jouguet principle which states that a transcritical front propagates with the minimal admissible velocity [19].

*If the wave travels to the rightwards direction, as we assume without any loss of generality.

After some computations the ODEs System (3.11) – (3.14) can be reduced to a single differential equation with implicit dependence on ξ:

$$\frac{\mathrm{d}q}{\mathrm{d}u} = \frac{\sigma}{2} \frac{\overbrace{\left(u^2 - (1+\delta)\,q^2 - m\right)}^{\stackrel{\text{def}}{=:}\ \mathscr{A}(q,\,u)} \cdot \overbrace{\left((u-c)^2 - m\right)}^{\stackrel{\text{def}}{=:}\ \mathscr{D}(u)}}{(u-c)^2 \cdot \underbrace{\left(\alpha m - \sigma q \cdot \left(u + \frac{m}{2\,(u-c)}\right)\right)}_{\stackrel{\text{def}}{=:}\ \mathscr{B}(q,\,u)}}, \tag{3.15}$$

where the expression for $m(\xi)$ in terms of $u(\xi)$ is obtained by integrating equation (3.12):

$$m(\xi) = -\frac{\mathcal{M}(c)}{u(\xi) - c}. \tag{3.16}$$

The integration "constant" $\mathcal{M}(c)$ can be determined from the Rankine–Hugoniot conditions written at the wave front [47, 72].

3.3.2 Stability of equilibria

In this Section we study the existence and stability of equilibria points to Equation 3.15. One of the difficulties is that the right hand side depends on a free parameter δ, whose variation has to be taken into account. The wave celerity $c > u$ has to be specified as well.

As the first step, we rewrite equation (3.15) as a dynamical system in the plane $(q,\,u)$ with ξ being the evolution variable:

$$\begin{aligned} q' &= \sigma\,\mathscr{A}(q,\,u)\,\mathscr{D}(u) \stackrel{\text{def}}{=:} \mathscr{F}_q(q,\,u), \\ u' &= 2\,(u-c)^2\,\mathscr{B}(q,\,u) \stackrel{\text{def}}{=:} \mathscr{F}_u(q,\,u). \end{aligned}$$

The equilibria points might be of two kinds:

(1) On the intersection of curves $\Gamma_{\mathscr{A}} \stackrel{\text{def}}{:=} \{\mathscr{A}(q,\,u) = 0\}$ and $\Gamma_{\mathscr{B}} \stackrel{\text{def}}{:=} \{\mathscr{B}(q,\,u) = 0\}$
(2) On the intersection of $\{\mathscr{D}(u) = 0\}$ and $\{\mathscr{B}(q,\,u) = 0\}$

The linear stability of equilibria is determined by eigenvalues of the following Jacobian matrix:

$$\mathscr{J}(q,\,u;\,\delta,\,c) \stackrel{\text{def}}{:=} \begin{pmatrix} \dfrac{\partial \mathscr{F}_q}{\partial q} & \dfrac{\partial \mathscr{F}_q}{\partial u} \\ \dfrac{\partial \mathscr{F}_u}{\partial q} & \dfrac{\partial \mathscr{F}_u}{\partial u} \end{pmatrix}. \tag{3.17}$$

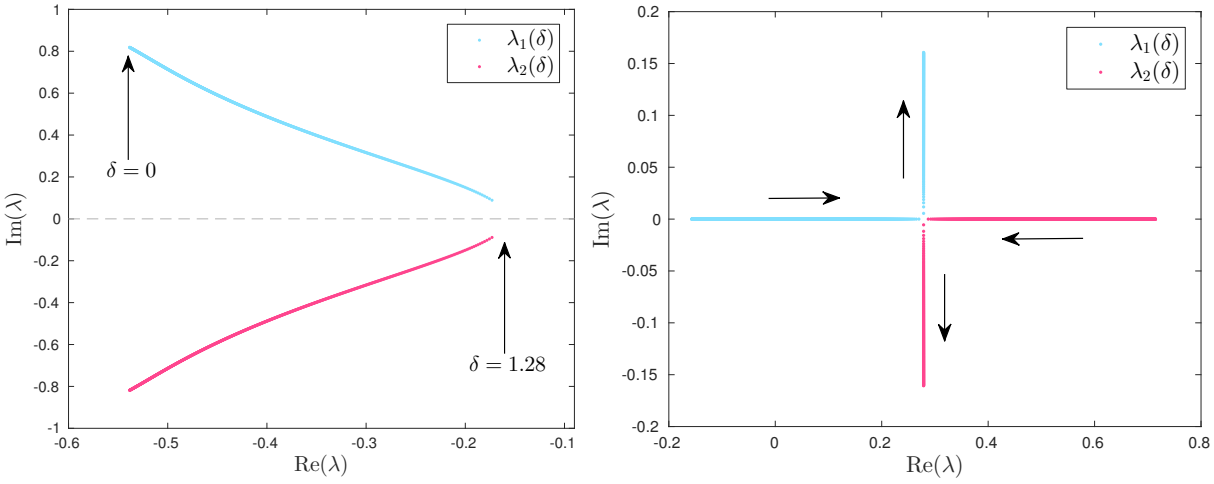

Figure 5. *Eigenvalues of the* JACOBIAN (3.17) *for various values of the parameter* $\delta \in [0, 1.28]$. *The left and right panels (a, b) correspond to equilibria of the first and second kinds correspondingly. Eigenvalue positive real part indicates the instability of the equilibrium point [79]. The arrows in the right panel indicate the increasing direction of the parameter* δ.

The elements of the JACOBIAN can be computed by direct differentiation:

$$
\begin{aligned}
\mathscr{J}_{11} &= -2\,\sigma\,(1 + \delta)\,q\,\mathscr{D}(u)\,,\\
\mathscr{J}_{12} &= \sigma\left[\left[2\,u - \frac{\mathcal{M}}{(u-c)^2}\right] + \left[2\,(u-c) - \frac{\mathcal{M}}{(u-c)^2}\right]\mathscr{A}(q,u)\right],\\
\mathscr{J}_{21} &= -\sigma\,(u-c)^2\left[2\,u - \frac{\mathcal{M}}{(u-c)^2}\right],\\
\mathscr{J}_{22} &= 4\,(u-c)\,\mathscr{B}(q,u) + 2\left(\alpha\,\mathcal{M} - \sigma\,q\,\mathscr{D}(u)\right).
\end{aligned}
$$

The last expression can be simplified at equilibria locations by taking into account the fact that $\mathscr{A} = \mathscr{B} \equiv 0$ at the first kind and $\mathscr{D} = \mathscr{B} \equiv 0$ at equilibria states of the second kind.

Eigenvalues $\lambda_{1,2}(\delta)$ of the JACOBIAN matrix $\mathscr{J}$ as functions of the parameter δ for both types of equilibria points are shown in Figure 5. The physical parameters used in this numerical computation are $\sigma = 0.15$, $\alpha = \tan\varphi = 1.0$, $c = 2.787$ and $\mathcal{M} = 0.1\,c$. From this illustration it is clear now that, at least for these values of parameters, the equilibria of the first kind are unstable spiral points, while the equilibria of the second kind are (linearly) stable spirals [79].

3.3.3 A particular class of travelling waves

Similarly to the construction of steady solutions presented in the previous Section 3.2, we are looking for *travelling wave solutions* to system (2.42) – (2.45) of the form:

$$h(t,\,x) \;=\; h(\xi)\,, \quad u(t,\,x) \;=\; u(\xi)\,, \quad m(t,\,x) \;=\; m(\xi)\,,$$

where $\xi \;\equiv\; x \;-\; c\cdot t$ is a combined independent variable introduced earlier. In other words, we consider the frame of reference where the travelling wave is steady. Notice that the model (2.42) – (2.45) does not possess the Galilean invariance property because of the velocity variables present in the right hand sides. This effect comes from the assumption that the ambient fluid remains in rest, which privileges this particular frame of reference. The constant $c \;>\; 0$ is the unknown wave celerity to be determined during the solution procedure.

Consider travelling waves of the following particular form:

$$u(\xi) \;=\; u_f\,, \quad m(\xi) \;=\; m_f\,, \quad q(\xi) \;=\; q_f\,, \quad h(\xi) \;=\; h_f \;-\; \varsigma\,\xi\,,$$

with $\varsigma \;>\; 0$ and $\xi \;<\; 0$. The travelling wave ansatz presented above satisfies the following relations:

$$\varsigma\cdot\big(c \;-\; u_f\big) \;=\; \sigma\cdot q_f\,, \tag{3.18}$$

$$\varsigma\cdot\big((c \;-\; u_f)\,u_f \;-\; \tfrac{1}{2}\,m_f\big) \;=\; \alpha\cdot m_f\,, \tag{3.19}$$

$$\varsigma\cdot\big((c \;-\; u_f)\cdot\big(u_f^2 \;+\; q_f^2 \;+\; m_f\big) \;-\; m_f\cdot u_f\big) \;=\; 2\,\alpha\, m_f\cdot u_f \;-\; \kappa\cdot q_f^3\,. \tag{3.20}$$

We use also an additional hypothesis that the flow in the coordinate frame moving with the travelling wave is critical, *i.e.*

$$\big(u_f \;-\; c\big)^2 \;=\; m_f\,. \tag{3.21}$$

The last condition can be equivalently recast as

$$\mathrm{Fr}_f \;\stackrel{\text{def}}{:=}\; \frac{|\,c \;-\; u_f\,|}{\sqrt{m_f}} \;\equiv\; 1\,,$$

where Fr_f is the Froude number with respect to the wave front [38]. This condition ensures the existence of the self-sustained regime of the wave propagation independently of small perturbations which might occur behind the wave front. It is completely analogous to the so-called Chapman–Jouguet condition for the propagation of a self-sustained detonation wave in gas dynamics [119].

The wave celerity c might be eliminated from Equations (3.18) – (3.21) by introducing new variables:

$$u^\star \;\stackrel{\text{def}}{:=}\; \frac{u_f}{c}\,, \qquad q^\star \;\stackrel{\text{def}}{:=}\; \frac{q_f}{c}\,, \qquad m^\star \;\stackrel{\text{def}}{:=}\; \frac{m_f}{c^2}\,.$$

As a result, we come to the following closed system of equations:

$$\varsigma \cdot (1 - u^\star) = \sigma \cdot q^\star , \tag{3.22}$$

$$\varsigma \cdot (1 - u^\star)\, u^\star - \tfrac{1}{2}\, \varsigma \cdot m^\star = \alpha \cdot m^\star , \tag{3.23}$$

$$\varsigma \cdot \left((u^\star)^2 + (q^\star)^2 + m^\star \right) - \varsigma \cdot m^\star \cdot u^\star = 2\,\alpha\, m^\star \cdot u^\star - \kappa \cdot (q^\star)^3 , \tag{3.24}$$

$$\left(1 - u^\star\right)^2 = m^\star . \tag{3.25}$$

By assuming that $\sigma \cdot q^\star \neq 0$, from last equations we can derive a simple relation:

$$(u^\star)^2 - m^\star - (1 + \delta) \cdot (q^\star)^2 = 0 ,$$

and by using the scaled version (3.25) of relation (3.21), we obtain that

$$2\,u^\star - 1 = (1 + \delta) \cdot (q^\star)^2 ,$$

or formally,

$$q^\star = \sqrt{\frac{2\,u^\star - 1}{1 + \delta}} ,$$

provided that $u^\star > \frac{1}{2}$ so that the value $q^\star \in \mathbb{R}^+$. After dividing (3.23) by (3.22) we have:

$$\frac{(1 - u^\star)\, u^\star - \frac{1}{2}\, m^\star}{1 - u^\star} \equiv \frac{1}{2} \left(3\,u^\star - 1 \right) = \frac{\alpha \sqrt{1 + \delta}\, (1 - u^\star)^2}{\sigma \sqrt{2\,u^\star - 1}} .$$

In other words, we have the following equation for $u^\star$:

$$3\,u^\star - 1 = \beta\, \frac{(1 - u^\star)^2}{\sqrt{2\,u^\star - 1}} , \qquad \text{with} \qquad \beta \stackrel{\text{def}}{:=} \frac{2\,\alpha \sqrt{1 + \delta}}{\sigma} . \tag{3.26}$$

Under the same condition on $u^\star$, we can transform Equation (3.26) into the following algebraic equation:

$$(3\,u^\star - 1)^2 \cdot \left(2\,u^\star - 1 \right) = \beta^2 \cdot (1 - u^\star)^4 .$$

It can be shown (see Appendix A.2) that there exists a unique positive root to this equation, which belongs to the interval $u^\star \in (\frac{1}{2}, 1)$. All other remaining quantities such as ς, $m^\star$ and $q^\star$ are determined after finding $u^\star$. The velocity c can be found from the mass conservation equation written at the wave front:

$$(c - w_b) \cdot m_b + (c - u_f) \cdot m_f = c \cdot m_s , \qquad w_b > c .$$

If $m_s \equiv 0$, the last equation takes a particularly simple form:

$$\frac{(c - w_b)^3}{(U_b)^3} + \left(\mathrm{Fr}_b \right)^{-\frac{2}{3}} \frac{c}{U_b} - 1 = 0 ,$$

where we introduced some notations:

$$U_b \stackrel{\text{def}}{:=} \sqrt[3]{\mathcal{M}_b} , \qquad \mathrm{Fr}_b \stackrel{\text{def}}{:=} \frac{u_b}{\sqrt{m_b}} = \sqrt{\frac{\alpha}{c_w}} .$$

We remind that the positive constant c_w controls the magnitude of bottom friction effects. We thus arrive to the following cubic polynomial equation for the quantity $C \stackrel{\text{def}}{:=} \dfrac{c}{U_b}$:

$$\mathcal{P}(C) \equiv (1 - u^\star)^3 C^3 + \left(\mathrm{Fr}_b\right)^{-\frac{2}{3}} C - 1 = 0 .$$

It is not difficult to see that the polynomial $\mathcal{P}(C)$ is a monotonically increasing function of C provided that $u^\star \leqslant 1$ and, thus, there exists a unique positive root (since $\mathcal{P}(0) = -1 < 0$). The dependence of the computed in this way coefficient $C = C_e(\mathrm{Fr}_b) = C_e(\varphi)$ on the channel slope angle φ is shown in Figure 6 with the blue dashed line (for a fixed value of $c_w = 0.004$ and with $\sigma = 0.15$, $\delta = 4$). Note that in the experimental study [18] the notation $C \equiv \dfrac{c}{U_0}$ was used, while we consider another definition $C \equiv \dfrac{c}{U_b}$, where $U_0 \stackrel{\text{def}}{:=} \sqrt[3]{\mathcal{M}_0}$. We can see that this prediction does not compare very well with the experimental data [18, 46, 112, 118] for large slope angles φ. This drawback will be corrected below. The agreement for small angles of inclination is achieved since $\mathcal{M}_j \ll \mathcal{M}_b$ and, consequently, $U_0 - U_b \ll U_b$. Therefore, the total mass flux $\mathcal{M}_0$ can be replaced by the bottom flux $\mathcal{M}_b$ to find the density current head velocity. It is also worth to mention that the big scatter in experimental data depicted in Figure 6 can be also partly explained by the differences between the total $\mathcal{M}_0$ and bottom $\mathcal{M}_b$ mass fluxes, which depend on precise inflow conditions.

3.3.4 Further considerations

The stability of the constructed travelling wave solution with the linear growth of the profile (due to the perpetual entrainment of sediments and still water into the mixing layer) has to be studied separately. The constructed solution belongs to the important class of stratified flows with fluid particles (in some parts of this flow) moving faster than the wave front. It is known that for surface waves it leads to inevitable wave breaking [80]. The authors are not aware of any mathematical stability studies of such stratified flows.

In the modelling of density currents, where there is a heavy particle (of density ρ_0) entrainment into the flow, the "boundary" conditions imposed on the wave front have the capital importance. In the previous Section these conditions were determined by the flow structure and we saw that it leads to the poor prediction of the wave celerity comparing with experimental data [18, 46, 112, 118]. Here we propose another set of "boundary" conditions:

$$m \cdot (c - u) + b_0 \zeta_b \cdot (c - w_b) = 0 , \tag{3.27}$$

$$h \cdot \left((u - c)\, u + \tfrac{1}{2}\, m\right) = 0 , \tag{3.28}$$

$$\left(c - u\right)^2 = m , \tag{3.29}$$

which are composed of the mass conservation equation, the flow criticality condition relative to the wave front and also the momentum conservation equation. It is not difficult to see that for $u < c$, it follows that $u = \frac{1}{3}\, c$ and for the dimensionless combination $C = \frac{c}{U_b}$

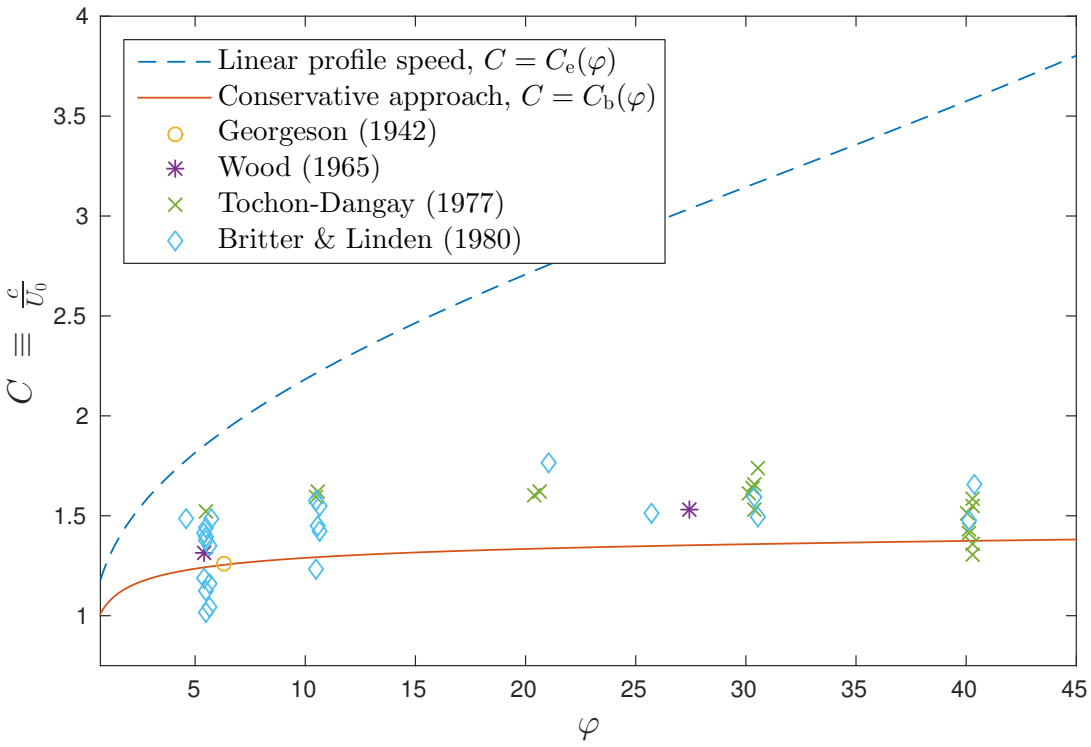

Figure 6. *Dependence of the flow head speed on the slope angle: analytical predictions against experimental measurements [18, 46, 112, 118]. The friction parameter used is* $c_w = 0.004$.

we obtain the following cubic equation:

$$\frac{8}{27}\, C^3 \;+\; \mathrm{Fr}_b^{-\frac{2}{3}}\, C \;-\; 1 \;=\; 0\,. \tag{3.30}$$

All intermediate computations are explained in Appendix B. For large values of the Froude number, the solution $C \approx 1.5$. This estimation is in good agreement with the empirical conjecture on the density current flow head velocity based on the experiments reported in [18]:

$$c \;\approx\; 1.5 \times \mathcal{M}_0^{\frac{1}{3}}\,.$$

In Figure 6 the solid line shows the dependence of the flow head celerity $C = C_b(\varphi)$ based on Equation (3.30). The overall good agreement of the lower solid curve with the experimental data [18, 46, 112, 118] certifies the model quality. It is worth to notice that the proportionality coefficient in experimental studies was determined based on velocity $\mathcal{M}_0^{\frac{1}{3}}$ and not on velocity U_b. As a result, for more accurate comparisons with considered models, one has to determine accurately, which part of the mass flow $\mathcal{M}_0$ entered into the boundary layer, since $U_b = \mathcal{M}_b^{\frac{1}{3}} = \left(\mu\,\mathcal{M}_0\right)^{\frac{1}{3}}$, with $\mu \leqslant 1$.

3.4. Similarity solutions

Additionally to special solutions considered in two previous Sections, System (2.42) – (2.45) admits also the following class self-similar solutions:

$$h(x,t) = t^{\theta+1}\hat{h}(\xi), \qquad u(x,t) = t^{\theta}\hat{u}(\xi),$$
$$m(x,t) = t^{2\theta}\hat{m}(\xi), \qquad q(x,t) = t^{\theta}\hat{q}(\xi), \quad (3.31)$$

where $\xi \overset{\text{def}}{:=} \dfrac{x}{t^{\theta+1}}$ and $\theta \in \mathbb{R}$. For flows with the sustained mass flow $\mathcal{M}_b \equiv \text{const}$ or with the sustained sediment mass $m_s \equiv \text{const}$, from conditions on the front it follows that $\theta \equiv 0$. For the sustained mass flow in the turbulent mixing layer $\mathcal{M}_j \equiv \text{const}$, the same value for θ follows from boundary conditions, *i.e.* $\theta \equiv 0$. Henceforth, for all just mentioned cases, we look for solutions of the form:

$$h(x,t) = t\cdot\hat{h}(\xi), \qquad u(x,t) = \hat{u}(\xi),$$
$$m(x,t) = \hat{m}(\xi), \qquad q(x,t) = \hat{q}(\xi), \quad (3.32)$$

with $\xi \overset{\text{def}}{:=} \dfrac{x}{t}$. Such solutions play a very important rôle in understanding the system (2.42) – (2.45), since dynamic solutions tend to self-similar ones at large times provided that constant mass fluxes are maintained.

Another important class of self-similar solutions (3.31) is realized when $\mathcal{M}_0 \equiv 0$, $m_s \equiv 0$. This corresponds to the evolution of a finite mass of a heavier liquid, which propagates under the layer of a lighter fluid. In this case, the mass conservation law

$$\int_0^{+\infty} m(t,x)\,\mathrm{d}x = \text{const}$$

yields self-similar solutions of the form (3.31):

$$h(x,t) = t^{2/3}\hat{h}(\xi), \qquad u(x,t) = t^{-1/3}\hat{u}(\xi),$$
$$m(x,t) = t^{-2/3}\hat{m}(\xi), \qquad q(x,t) = t^{-1/3}\hat{q}(\xi),$$

where $\xi \overset{\text{def}}{:=} \dfrac{x}{t^{2/3}}$. This self-similar solution indicates that the wave front position x_f behaves asymptotically in time as [105]:

$$x_f \propto t^{2/3}.$$

From the last estimation, the following asymptotic behaviour of the front velocity U_f can be readily deduced:

$$U_f \propto x_f^{-1/2}. \quad (3.33)$$

The last decay law was validated experimentally in [9, 81]. In the present work this asymptotic behaviour will be used to validate the numerical simulations. This approach to the description of turbidity currents is referred as the "*thermal theory*" [9].

In turbidity flows, in order to construct self-similar solutions for density currents along a slope (as well as for travelling waves), it is of capital importance to prescribe the *adequate*

boundary conditions. During the construction of travelling waves above, we see that the wave celerity depends on the relations imposed at the wave front. When the solution is given by ansatz (3.31), the flow head is uniquely determined. However, the applicability of such similarity solutions to flows in the absence of sediments (*i.e.* $m_s \equiv 0$, $\mathcal{M}_b \equiv 0$) has to be studied separately.

The situation changes when we consider the problem of sediments entrainment into the flow ($m_s > 0$, $\mathcal{M}_b \equiv 0$). In the framework of the conservative system (2.46) – (2.49) this problem can be interpreted as the mixed Initial–Boundary Value Problem (IBVP). Namely, at the initial moment of time we know the distribution of heavy sediments in the sediment layer $h_s(x)$, $m_s(x)$. The sediments might be at rest ($u_s(x) \equiv 0$) or moving with prescribed velocity $u_s(x)$ and turbulent kinetic energy $q_s(x)$. The perturbations entraining the sediments into the flow are entering the fluid domain from the left boundary (without any loss of generality). In Figure 1 we depicted the sketch of the fluid domain for an illustration. In this situation there is no need to separate the flow head and to write additional relations on the wave front, since the main flow characteristics are obtained in the process of solving the IBVP. However, the main question remains unanswered: which self-similar regime (3.31) will appear as the long time limit of the unsteady solution?

System (2.46) – (2.49) is of hyperbolic (and hydrodynamic) type and it corresponds to the flow of a barotropic gas with chemical reactions in compressible fluid dynamics. We have already mentioned above the analogy between density currents and the detonation theory. During the normal detonation, the fluid flow satisfying the Chapman–Jouguet conditions downstream the flow head is not always realized (especially in the presence of accompanying chemical reactions). Under certain conditions the wave of detonation might propagate with the velocity exceeding that of perturbations behind the wave front [41]. The main conclusion that we can draw from this analogy is that the realizability of self-similar solutions has to be studied separately. Such an analytical study might turn out to be very complex. Below we will show by numerical means that the propagation of the flow head with the speed higher than expected is possible. The similarity solutions described in this Section are validated below in Section 4.4. We would like to mention also that similarity solutions for gravity currents were constructed also in [105] and [62, Sections 3 & 4].

4. Model validation and unsteady simulations

Strictly speaking, we already validated steady solutions to System (3.2) – (3.7) by making comparisons with the experiments from [101]. We show that this system is able to predict qualitatively and quantitatively the development of the mixing layer over a slope.

4.1. Problem formulation

In this Section we continue the validations by considering unsteady solutions hereinafter. Moreover, we shall consider the applicability of an even simpler one-layer model (2.36) –

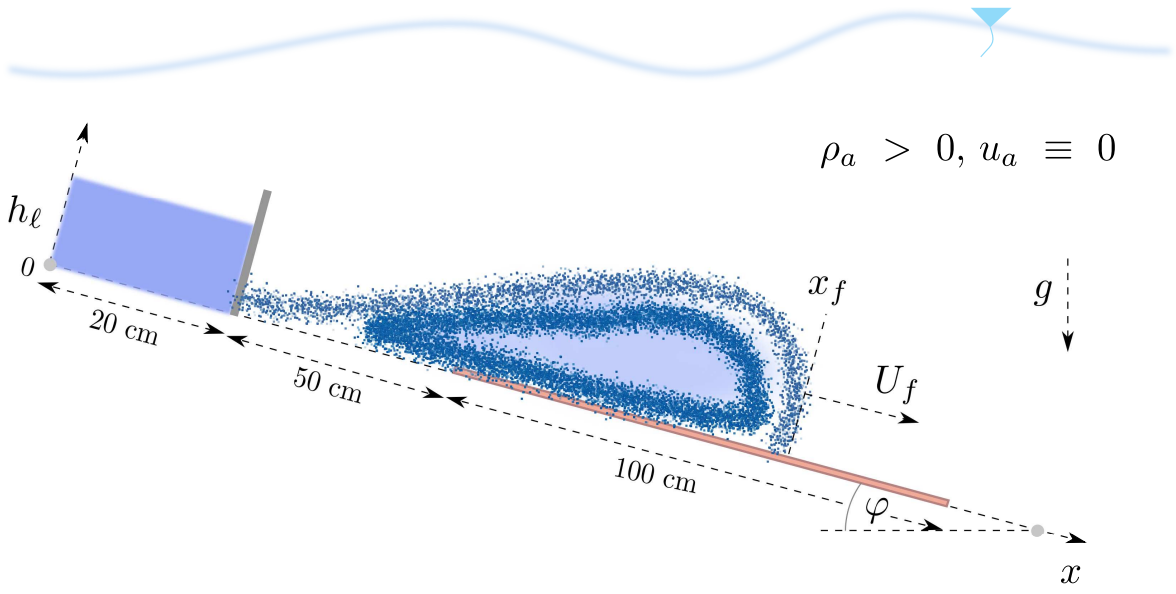

Figure 7. *Sketch of numerical lock-exchange experiments.*

(2.40). We apply it to simulate the sediments entrainment process by density currents over moderate (finite) slopes. Numerical solutions will be compared with experimental data reported in [103] as well as with exact special solutions of travelling wave type. In their experiments the dense fluid consisted either of saltwater or of the sawdust particle suspension. The shape of these particles was irregular in accordance with suspended snow flakes. The spatial growth of the cloud was determined from the side view images recorded with a video camera. A 5 cm square grid was drawn on the side glass to facilitate the front position determination. Moreover, we shall show below that under certain initial conditions the numerical solution will tend asymptotically to self-similar solutions described earlier.

We made our choice for experimental data of Rastello & Hopfinger (2004) [103] for the following reasons:

- This experiment corresponds fairly well to the scope and purpose of our numerical model
- The model (2.36) – (2.40) is suitable for the simulation of gravity currents even over moderate and large slopes used in the experimental study [103] (see Table 2 for the values of the slope parameter). When using other models, one has to check that the influence of the sediment bottom layer is taken into account to represent correctly the front dynamics
- The experiment was conducted for sufficiently long time. In this way we are able to check our model validity for the acceleration and deceleration stages of the flow. Finally, we were even able to check the asymptotic behaviour of the flow, which is very typical for buoyant flows over a slope.

We already mentioned above that the equilibrium system (2.36) – (2.40) possesses the hyperbolic structure similar to the equations of gas dynamics with two "sonic" and two

contact characteristics [47, 72]. There is a wide choice for the numerical discretization of such systems. However, taking into account that we deal with a system of conservation (balance) laws, it seems to be natural to opt for finite volume schemes [7]. Henceforth, in order to solve numerically the equilibrium system (2.36) – (2.40) we use the classical and robust finite volume discretization and the widely used Godunov scheme [48–50]. The explicit Euler scheme is used in time discretization.

Sketch of the numerical experiment is given in Figure 7. Our goal is to reproduce *in silico* some of the laboratory experiments reported in [103]. The values of all physical parameters are given in Table 2. The initial and boundary conditions are rather standard as well. Initially, at $t = 0$, the distribution of evolutionary quantities is given on the computational domain $[0, \ell]$:

$$h(x, 0) = h_0(x), \quad u(x, 0) = u_0(x), \quad m(x, 0) = m_0(x), \quad q(x, 0) = q_0(x).$$

On the right boundary we set wall boundary conditions for simplicity*. On the left extremity of the computational domain the boundary conditions depend on the flow regime in the vicinity of the left boundary. If the flow there is supercritical, we impose Cauchy's data. Otherwise, we impose a wall boundary condition as well. The case we study below is depicted in Figure 7 and it will be described in more details below.

4.2. Experimental set-up

In order to reproduce *in silico* the experiments of Rastello & Hopfinger (2004) [103] we use the following configuration of the numerical tank. The channel length ℓ is equal to 200 cm. As we already mentioned, on boundaries we impose wall boundary conditions, in other words the channel is closed as in experiments. A heavier fluid of buoyancy $b_\ell \in \{1, 19\}\ \frac{\mathsf{cm}}{\mathsf{s}^2}$ fills an initially closed container of the length of 20 cm and of variable height h_ℓ, which changed from one experiment to another. This configuration corresponds to the classical lock-exchange experiment. The heavy fluid "mass†" $m_\ell = b_\ell \cdot h_\ell$. At the distance of 50 cm from this recipient the slope is covered by initially motionless sediment layer of the height $\zeta_s = 0.2$ cm and 2 cm. The "mass" of sediments is $m_s = b_s \cdot \zeta_s$. The length of sediments layer is 100 cm. During the propagation of the heavy fluid head all these sediments were entrained into the flow. In some experiments the sediment layer was absent, *i.e.* $m_s \equiv 0$. In this case the flow simply propagates over the rigid inclined bottom. In order to avoid the degeneration of certain equations, in numerical experiments we cover the whole slope with a micro-layer of sediments with mass $m_s^\circ > 0$, such that

$$m_s^\circ \ll m_s \qquad \text{and} \qquad m_s^\circ \ll m_\ell.$$

The values of all physical parameters are given in Table 2. The influence of the model parameters on predicted values was found to be rather weak. Consequently, in all numerical

*In any case, the simulation stops before the mass reaches the right boundary. So, the influence of the right boundary condition on presented numerical results is completely negligible.

†We employ the term mass in the sense of the relative weight of the dense fluid.

Parameter	*Experiment 1*	*Experiment 2*
Slope angle, φ	32°	45°
Container height, h_ℓ	6.5 cm	20 cm
Heavy fluid buoyancy, b_ℓ	19 $\frac{\mathsf{cm}}{s^2}$	1 $\frac{\mathsf{cm}}{s^2}$
Sediment deposit height, ζ_s	0.2 cm	2.0 cm
Minimal sediment "mass", m_s°	10^{-3} $\frac{\mathsf{cm}^2}{\mathsf{s}^2}$	10^{-3} $\frac{\mathsf{cm}^2}{\mathsf{s}^2}$
Sediment "mass", m_s	10 $\frac{\mathsf{cm}^2}{\mathsf{s}^2}$; 20 $\frac{\mathsf{cm}^2}{\mathsf{s}^2}$	3 $\frac{\mathsf{cm}^2}{\mathsf{s}^2}$
Final simulation time, T	10 s	20 s

Table 2. *Parameters used in numerical simulations of the experiments from* Rastello & Hopfinger *(2004) [103, Table 2], schematically depicted in Figure 7.*

simulations reported below we used the following values of these parameters:

$$\sigma \;=\; 0.15\,, \qquad \delta \;=\; 0\,, \qquad c_w \;=\; 0\,.$$

The results of the critical comparisons with laboratory data are discussed below.

4.3. Numerical results

In Figure 8 we report the results of numerical simulations showing the spatial profiles of four quantities h, u, m and q. These simulations were performed without the sediments layer, *i.e.* $m_s \;\equiv\; 0$. The panels correspond to:

Left panel: Slope angle $\varphi \;=\; 32^\circ$, the snapshot is taken at $T \;=\; 10\,\mathsf{s}$

Right panel: Slope angle $\varphi \;=\; 45^\circ$, the snapshot is taken at $T \;=\; 20\,\mathsf{s}$.

All quantities reported in Figure 8 are given in dimensional variables. The position of the density current front is clearly visible in both cases despite the fact that the IBVP was solved in the domain $[\,0,\,\ell\,]\times[\,0,\,T\,]$ using simple shock-capturing methods (*i.e.* no special treatment was necessary to detect the front). This property of the employed numerical scheme will be used to analyze below the asymptotic behaviour of unsteady solutions.

In Figure 9 we show the dependence of the flow head velocity U_f on the distance x_f traveled by the front. The parameters of these numerical/laboratory Experiments 1 & 2 are given in Table 2. Please, note that the heavy fluid density in Experiment 1 is much higher. The last observation explains why the head velocity in Experiments 1 is higher than in Experiments 2, even if the slope is bigger in Experiments 2. Various symbols

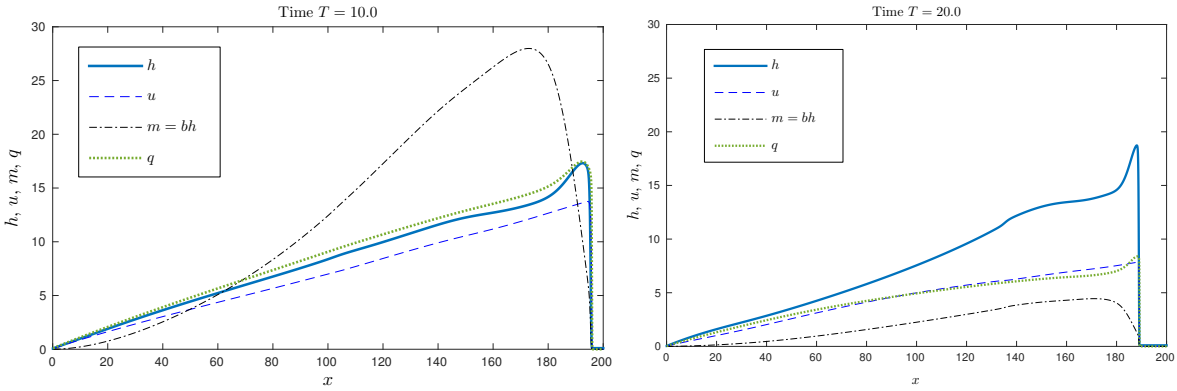

(a) $\varphi = 32°$ (b) $\varphi = 45°$

Figure 8. *Distribution of depth-integrated physical quantities h, u, m and q in numerical computations reproducing the experimental set-up from [103]. These simulations are performed without the presence of sediments along the slope.*

(◯ and ▽) correspond to laboratory measurements of the head velocity and are taken from [103, Fig. 11]. Solid and dash-dotted lines (with ◯ and ▽) indicate the experiments with ($m_s > 0$) and without ($m_s = 0$) sediments correspondingly. The presence of sediments before the head front yields the initial acceleration of the flow. This acceleration phase is followed by deceleration, since sediments are distributed over a limited distance in our experiments. A very good agreement with numerical predictions can be observed in Figure 9.

In Figure 10 we show the long time behaviour of the front velocity from the Experiment 2 reported in Figure 9 with parameters from Table 2. In order to perform this simulation we increased the computational domain* from 200 to 500 cm. Sediments were absent along the slope in this computation (*i.e.* $m_s \equiv 0$). The excellent agreement with theoretically established asymptotics $U_f \sim \dfrac{1}{\sqrt{x_f}}$ can be observed in this Figure 10. It validates both the numerics and the underlying theoretical argument.

4.4. Similarity solutions validation

In the previous Section in Figure 10 we demonstrated how an unsteady solution ($\mathcal{M}_j = 0$ and $m_s = 0$) tends to the asymptotic regime (3.33). If we assume that sediments are distributed uniformly along the slope ($m_s \equiv \text{const} \geqslant 0$) and initially they remain in the motionless equilibrium state (until the arrival of the density current), then, the asymptotic state of the unsteady solution is described by the similarity ansatz (3.32). In order to demonstrate this property, we consider the same experimental set-up depicted in Figure 7. However, in order to study long time behaviour of the flow, we consider the channel of the

*This operation can be made easily in numerical experiments contrary to laboratory experiments, where the channel size is rather fixed.

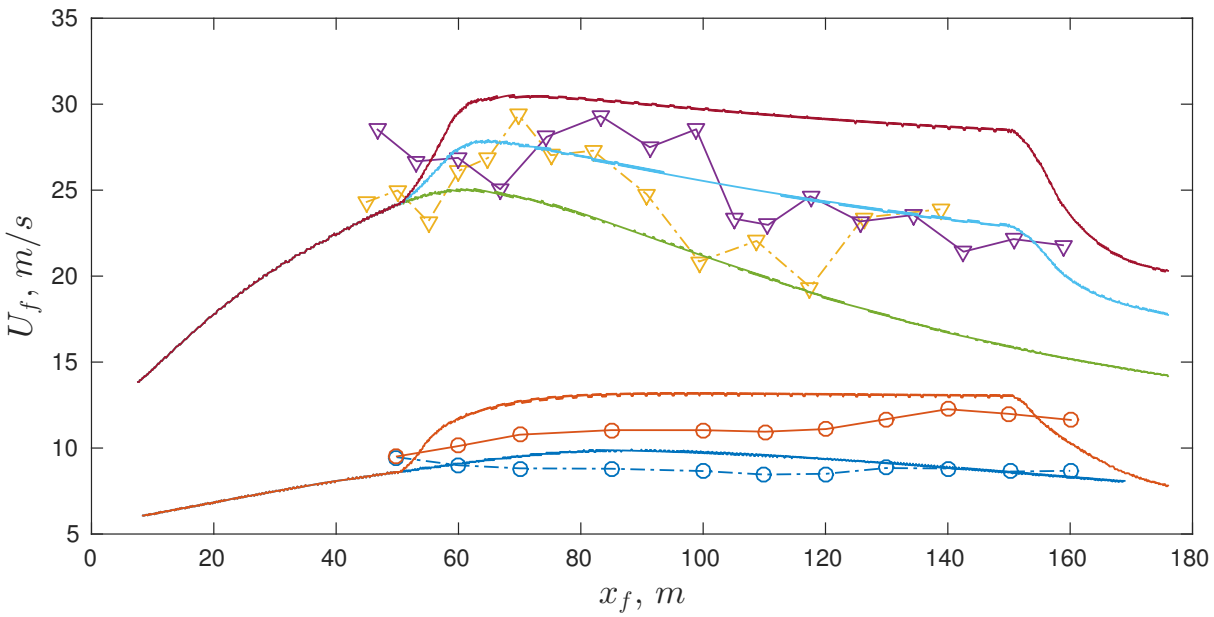

Figure 9. *Evolution of the front velocity U_f of laboratory clouds as a function of downstream distance x_f. Comparison of the predicted flow head velocity against the experimental results from Rastello & Hopfinger (2004) [103, Fig. 11]. The upper (lower) group of data corresponds to Experiment 1 (2) from Table 2 correspondingly.*

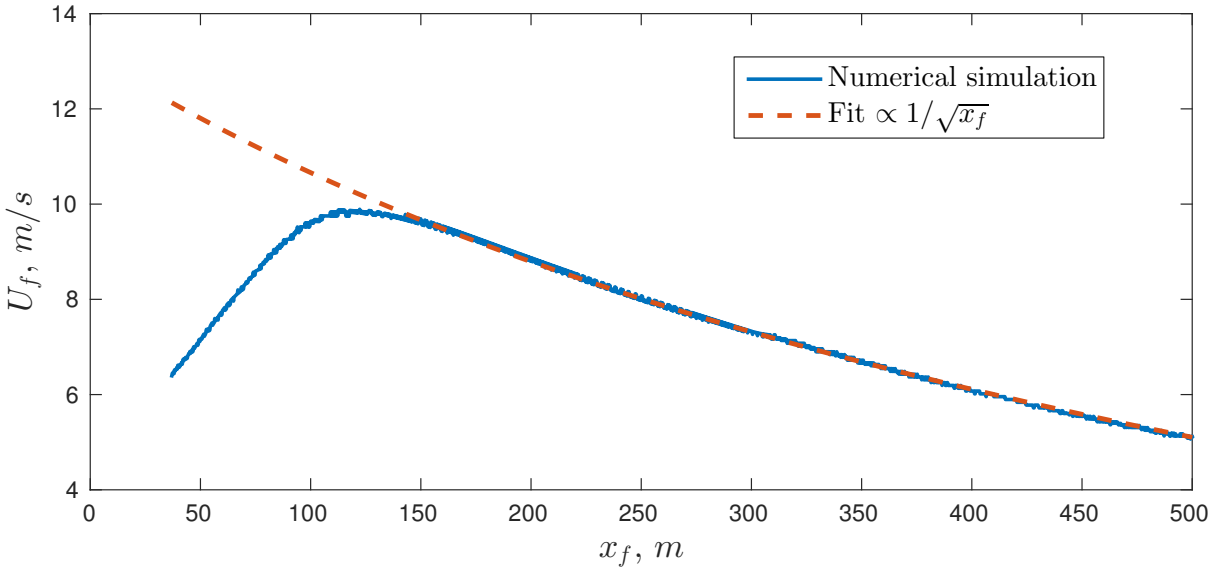

Figure 10. *Asymptotic behaviour (3.33) of the front velocity for the experiment 2 from Table 2.*

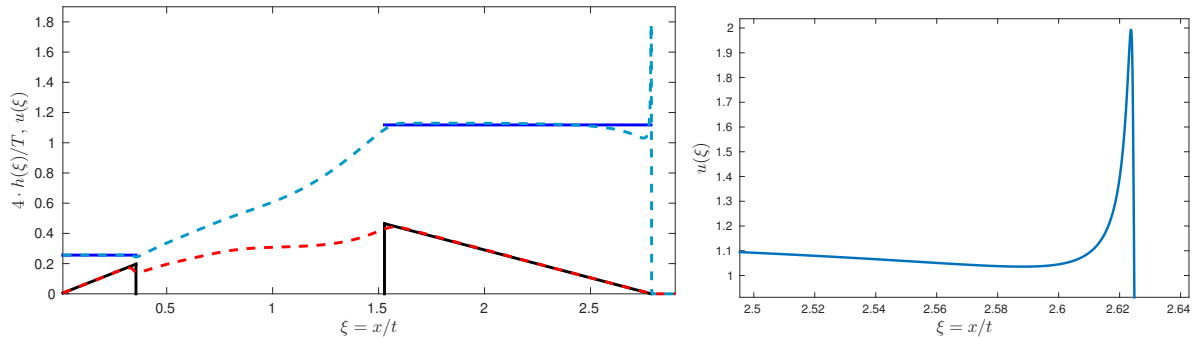

(a) (b)

Figure 11. *Validation of similarity solution by unsteady simulations. Left panel (a): the exact solution is depicted with solid lines (black — scaled flow height* $4\,\frac{h(\xi)}{T}$ *, blue —* $u(\xi)$*) and unsteady numerical prediction are shown with dashed lines (red — layer height, blue — horizontal speed). Right panel (b): zoom on the jump in the velocity variable at the flow head.*

length $\ell = 6\,000$ cm. The left channel boundary coincides with the origin of a CARTESIAN coordinate system $x = 0$ cm. The horizontal axis $O\,x$ is directed along the bottom. The vertical axis $O\,y$ is directed upwards in the direction orthogonal to the slope. The bottom slope is taken here to be $\varphi = 45°$. Starting from $x = 20$ cm and until the channel end a uniform ($h_s \equiv 0.1$ cm) motionless ($u_s \equiv 0$, $q_s \equiv 0$) layer of sediments of mass $m_s \equiv 0.1\ \frac{\text{cm}^2}{\text{s}^2}$ is located. Sediment particles start to move when the flow head passes and the layer depth increases to $h = 1.1\,h_s$. In order to initiate a *substantial* density flow in the channel after releasing the heavy fluid, it is sufficient to fill the reservoir located for $x \in [\,0,\,20\,]$ with the following heavy fluid parameters:

$$m_\ell = m_s\,, \qquad h_\ell = 1.2\,h_s\,, \qquad u_\ell = 0\,, \qquad q_\ell = 0\,.$$

For $t \gtrsim 1000$ s the numerical solution enters into the asymptotic regime (3.32) and for all subsequent times the flow picture does not change. The numerical solution for $T = 2000$ s is shown in Figure 11. The dashed lines on the left panel (a) show the theoretical distributions of the scaled wave height $4\,\frac{h\,(\xi)}{T}$ (red line) along with the velocity profile $u\,(\xi)$ (blue line). In numerical simulations we observed the flow head propagation speed $c_{\text{num}} \approx 2.79\ \frac{\text{cm}}{\text{s}}$. We remark that behind the wave front there is a sufficiently long zone $1.53 \approx \xi_1 < \xi < c_{\text{num}}$, where the solutions can be very well approximated by linear functions. In this area the wave profile is linear and the velocity is constant. A zoom on the velocity peak at the flow head is shown in the right panel of Figure 11(b). Its structure is quite smooth, when the flow is resolved to high resolution.

If at the left boundary of the channel we maintain the constant mass flux $\mathcal{M}_j$ (we take $\mathcal{M}_j \equiv 2.5\times10^{-3}\ \frac{\text{cm}^3}{\text{s}^3}$), then, in the neighbourhood of the left boundary another zone with the linear wave profile and constant velocity is formed. In our numerical simulations this zone occupies the interval $0 < \xi < \xi_0 \approx 0.355$. The flow in this area is supercritical

($u^2 > m$). Consequently, on the left boundary $x = 0$ we have to specify all evolution variables:

$$h_\ell = 0.005\,\mathsf{cm}\,, \qquad u_\ell = 0.5\,\frac{\mathsf{cm}}{\mathsf{s}}\,, \qquad m_\ell = 0.005\,\frac{\mathsf{cm}^2}{\mathsf{s}^2}\,, \qquad q_\ell = 0\,\frac{\mathsf{cm}}{\mathsf{s}}\,.$$

For $\xi_1 < \xi < c_{\text{num}}$ the flow is supercritical in the frame of reference moving with the flow head, *i.e.* $(c_{\text{num}} - u)^2 > m$. That is why behind the wave front the analogue of Chapman–Jouguet conditions are not verified.

In Section 3.2 some stationary solutions of the form

$$u \equiv u_j\,, \qquad m \equiv m_j\,, \qquad q \equiv q_j\,, \qquad h \equiv \varsigma_j \cdot x$$

were constructed. These solutions can be used to describe the flow on the interval $(0,\, \xi_0)$. Here the value of ξ_0 coincides with the characteristics, *i.e.* $\xi_0 = u_j + \sqrt{m_j}$. The corresponding solutions on this interval are shown in Figure 11 with solid lines. On the other hand, the travelling wave solutions with linear profiles constructed in Section 3.3.3 are not suitable in this situation, since the assumption about the critical character of the flow right behind the flow head is not verified in our numerical simulation. However, the last assumption can be relaxed. Let us consider an exact travelling wave solution of the following form:

$$h\,(t,\,x) = t\,\varsigma_f\,(c - \xi)\,, \qquad u\,(t,\,x) = u_f\,, \qquad m\,(t,\,x) = m_f\,, \qquad q\,(t,\,x) = q_f\,,$$

where c is the prescribed front celerity. Then, if we take $c = c_{\text{num}}\,,\, \xi_1 = u_f + \sqrt{m_f}\,,$ it can be easily checked that the above solution corresponds fairly well to the unsteady solution shown in Figure 11. In order to obtain the exact solution, we have to find the intersection in the plane $(q,\, u)$ of two curves $\Gamma_{\mathscr{A}}$ and $\Gamma_{\mathscr{B}}$ defined earlier in Section 3.3.2 (see also Section 3.3.1 for the motivation of these definitions):

$$\begin{aligned} u^2 - m - (1 + \delta)\,q^2 &= 0\,, && \left(\Gamma_{\mathscr{A}}\right) \\ \alpha\, m - \sigma\, q\left(u - \frac{m}{2\,(c - u)}\right) &= 0\,. && \left(\Gamma_{\mathscr{B}}\right) \end{aligned}$$

Using the relation $m = \dfrac{\mathcal{M}}{c - u}$ and the mass conservation condition at the wave front, we have

$$\mathcal{M} = (c - u)\,m = c\,m_s\,.$$

For parameter values used in our simulations, there exists a unique intersection point of curves $\Gamma_{\mathscr{A}}$ and $\Gamma_{\mathscr{B}}$, which satisfies the condition $(c - u_f)^2 > m_f$.

In general, the questions of long time behaviour of unsteady solutions and the attraction property of similarity flows cannot be answered without a thourough additional scientific investigation. In particular, similar to the detonation theory [41], it is necessary to formulate a criterium for the density current head front celerity selection. This celerity will determine the location of the wave front on large time intervals. Moreover, this celerity is a key parameter for evaluating the extent to which suspended material travels.

5. Discussion

Above we have proposed and tested a new model for density currents. We outline below the main conclusions and perspectives of this study.

5.1. Conclusions

In the present study we considered the problem of density current modelling propagating down the slope in the presence of sediment deposits on the rigid bottom. In order to describe this flow in mathematical terms, we divide it into three zones (from the bottom vertically upwards): the layer of sediments (i), the mixing layer (ii) and the still water layer (iii). In order to simplify the mathematical description, we assumed that the upper layer (iii) of the still water was motionless. The depth-averaged description was adopted in each of two remaining layers (i) and (ii). As a result, we arrived to a shallow water two-layer system including turbulent modelling, which can be recast in a conservative form (2.22) – (2.27) of hyperbolic balance laws [72]. The initially proposed system contains only six evolution equations to describe the complex density current. However, it can be further simplified if we assume that the flow in the bottom layer occupied by dense liquid or suspension with uplifted sediments is in the equilibrium state, *i.e.* the gravity force is exactly balanced by the friction forces with the rigid bottom. In this way, we can remove one equation corresponding to the bottom layer (i). The sediment equilibrium model is given by System (2.36) – (2.40). This concludes the modelling part of our study.

Then, the proposed equilibrium model is studied using analytical means. Namely, we were interested in some special, but very important classes of solutions — steady states, travelling waves and similarity flows. The linear stability of travelling waves was studied. The initial conditions which yield asymptotically (in time) some special solutions (such as self-similar and travelling waves) were discussed. The velocity of travelling waves is of capital importance for the understanding of turbidity flows propagation. Namely, the travelling wave speed gives an estimation of the flow head propagation along the slope. This prediction of our travelling wave analysis was checked against the experimental data from numerous previous studies [18, 46, 112, 118].

The mixing layer formation was discussed in the framework of steady solutions and our theoretical prediction was compared against experimental data from [100]. Moreover, unsteady solutions predicted by our model were compared with density flow experiments made in the LEGI laboratory by Rastello & Hopfinger (2004) [103]. The model predictions are in good agreement with their measurements of the front velocity. Finally, the asymptotic behaviour for the flow head velocity as a function of the front position was measured in our numerical computations and an excellent agreement was found with existing theoretical estimations. This concludes the validation of the model and also of several particular solutions derived in this study.

5.2. Perspectives

In the present study, we have employed only basic legacy first order GODUNOV finite volume schemes [48–50]. Their principal advantages are the ease of implementations and the robustness of numerical results. However, the accuracy might be also important in some applications, where a quantitative prediction is critically important. Consequently, some high order finite volume well-balanced schemes have to be developed to solve numerically the density current models proposed in our study. This technology is relatively well mastered nowadays [29–31, 51].

The system of equations presented earlier in this article is a simplified equilibrium model based on a number of physical assumptions. Of course, more complete models of higher physical fidelity should be developed as well in the future along the lines outlined in the monograph [75]. For instance, in this manuscript we considered density currents with uniform cross-sections, *i.e.* 2D flows. In future works 3D effects have to be included. Moreover, in all examples considered earlier, the uniform bed slopes was used. In part, it comes from the experimental set-up used in previous investigations. However, in upcoming works the interaction between the fluid flow with the bed morphology has to be investigated to advance our understanding of these processes.

Acknowledgments

This research was supported by the project AVAL (AAP MONTAGNE 2015, University Savoie Mont Blanc) and Russian Science Foundation (project 15-11-20013). V. LIAPIDEVSKII acknowledges the CNRS/ASR Cooperation Program under the project №23975 and the hospitality of the University Savoie Mont Blanc during his numerous visits. The authors are grateful to Professors L. ARMI & G. PAWLAK for their help in preparing this manuscript.

A. An exact solution

In the Appendix we present the construction of a particular steady solution. Using the information presented above in Sections 3.2 and 3.3, we construct in this Section the profile of a particular exact solution to Equations (2.42) – (2.45). We assume that in the bottom layer $\zeta \equiv \zeta_b$ and $w \equiv w_b$. Moreover, we suppose that the *total* mass inflow $\mathcal{M}_0 = b_0\,\zeta_0\,w_0$ is prescribed on the left boundary. This incident mass flux $\mathcal{M}_0$ splits into two streams:

$$\mathcal{M}_0 = \mathcal{M}_j + \mathcal{M}_b\,, \qquad \mathcal{M}_j \overset{\text{def}}{:=} \frac{1}{2}\,b_0\,h_L\,u_L\,, \qquad \mathcal{M}_b \overset{\text{def}}{:=} b_0\,\zeta_b\,w_b\,.$$

We assume also that the ratio $\mu \overset{\text{def}}{:=} \dfrac{\mathcal{M}_j}{\mathcal{M}_0} \in (0,\,1]$ is fixed. Thus, $\mathcal{M}_b$ can be also easily deduced.

The flow at any fixed moment of time $t = t_m > 0$ is composed of two parts:

(1) **Stationary flow:** $u(x,\,t) \equiv u_j$, $m(x,\,t) \equiv m_j$, $q(x,\,t) \equiv q_j$ and $h(x,\,t) = h_j + \varsigma_j \cdot x$, where $x \in [\,0,\,L_j\,]$, $L_j = u_j \cdot t_m$.

(2) **Travelling wave:** This part depends on the variable $\xi = x - c{\cdot}t$ and $u(\xi) \equiv u_f$, $m(\xi) \equiv m_f$, $q(\xi) \equiv q_f$ and $h(\xi) = h_f - \varsigma_f \cdot (x - L_t)$, where $\varsigma_f > 0$, $L_t - L_f \leqslant x \leqslant L_t$ and $L_f \overset{\text{def}}{:=} u_f \cdot t_m$, $L_t \overset{\text{def}}{:=} c \cdot t_m$.

The problem consists in finding all solution parameters. The solution algorithm is summarized below.

A.1. Steady flow

Let $a \overset{\text{def}}{:=} \dfrac{u_j}{U_j}$ be the ratio of two speeds with $U_j = \sqrt[3]{\mathcal{M}_j}$ and $z \overset{\text{def}}{:=} a^3$. Then, one has to find the unique root $z > 1$ to the following equation:

$$\left(1 - \frac{1}{z}\right) \cdot (1 + 2\,z)^2 = \frac{4\,\alpha^2\,(1+\delta)}{\sigma^2} \overset{\text{def}}{=:} \beta^2\,,$$

which is to be compared with Equation (3.26). It is equivalent to finding the root to the following cubic polynomial:

$$\mathcal{P}_1(z) = 4\,z^3 - (3 + \beta^2)\,z - 1\,.$$

Let $z^\star$ be the required root. Then, we find $a = \sqrt[3]{z^\star}$ and $u_j = a\,U_j$. We know that $\mathcal{M}_j = U_j^3 = m_j\,u_j$. Hence, $m_j = \dfrac{U_j^2}{a}$. The remaining variables are:

$$q_j = \sqrt{\frac{u_j^2 - m_j}{1+\delta}}\,, \qquad \varsigma_j = \frac{\sigma \cdot q_j}{u_j}\,, \qquad b_L = \frac{b_0}{2}\,, \qquad h_L = \frac{m_j}{b_L}\,.$$

Finally, the steady part of the turbulent jet layer depth is equal to

$$h(x,\,t) = h_L + \varsigma_j \cdot x\,, \qquad 0 \leqslant x \leqslant L_j = u_j \cdot t_m\,.$$

A.2. Travelling waves

For the travelling wave part we have $\mathcal{M}_b = U_b^3$ and $\mathrm{Fr}_b \overset{\text{def}}{:=} \dfrac{w_b}{\sqrt{b_0\,\zeta_b}}$. Let $u^\star \overset{\text{def}}{:=} \frac{u_f}{c}$ be the dimensionless flow velocity. It can be found by solving the following algebraic equation, which possesses a real root on the interval $u^\star \in \left(\frac{1}{2},\,1\right)$:

$$\mathcal{P}_2(u^\star) = \beta^2\,(1-u^\star)^4 - (2\,u^\star - 1)\,(3\,u^\star - 1)^2 = 0\,,$$

where the constant β was defined earlier in (3.26). The polynomial $\mathcal{P}_2(u^\star)$ can be expanded:

$$\mathcal{P}_2(u^\star) = (u^\star)^4 - (4 + 18\,\beta^{-2})(u^\star)^3 + (6 + 21\,\beta^{-2})(u^\star)^2 - (4 + 8\,\beta^{-2})\,u^\star + 1 + \beta^{-2}.$$

Let us assume that we have found the required root $u^\star \in \left(\frac{1}{2}, 1\right)$. Then, we solve another polynomial equation to determine $C = \frac{c}{U_b}$:

$$\mathcal{P}_3(C) = (1 - u^\star)^3 C^3 + \mathrm{Fr}_b^{-2/3} C - 1 = 0.$$

The last equation admits a unique positive root $C^\star = C^\star(\mathrm{Fr}_b) = C_e(\varphi)$ as well. The last dependence is shown in Figure 6 with the dashed line. Then, we consider the flow in the bottom layer. We have the following relations:

$$\mathcal{M}_b = b_0\,\zeta_b\,w_b \equiv U_b^3, \qquad w_b = \mathrm{Fr}_b\sqrt{b_0\,\zeta_b} \equiv \mathrm{Fr}_b\sqrt{m_b},$$

$$m_b = \mathrm{Fr}_b^{-2/3}\cdot\mathcal{M}_b^{2/3}, \qquad \zeta_b = \frac{m_b}{b_0}.$$

We can notice that w_b can be also written as $w_b = \mathrm{Fr}_b^{2/3} U_b$. Now we come back to the travelling wave:

$$c = C^\star U_b, \qquad u_f = u^\star c,$$

and from the relation

$$(c - u_f)\cdot b_0\,h_f = (w_b - c)\cdot m_b$$

we can find

$$h_f = \frac{(w_b - c)\cdot m_b}{(c - u_f)\cdot b_0},$$

provided that $(c - u_f)\cdot b_0 \neq 0$. Finally, we find two last elements of the solution:

$$q_f = \sqrt{\frac{2\,\dfrac{u_f}{c} - 1}{1 + \delta}}, \qquad \varsigma_f = \frac{\sigma\,q_f}{c - u_f}.$$

The travelling wave profile is then given by

$$h(\xi) = h_f - \varsigma_f\cdot(x - L_t), \qquad L_t = c\cdot t_m, \qquad L_f = u_f\cdot t_m.$$

The last profile is located in the segment $x \in [L_t - L_f, L_t]$. The solution exists if $u_j \leqslant u_f$. We underline that in the region between the stationary and travelling wave parts the flow in general is unsteady. Thus, the indicated boundaries $L_t - L_f$ and L_t are rather approximations to the reality. Two such exact solutions for two different values of the parameter $\mu = 0.05$ (left panel) and $\mu = 0.654$ (right panel) are depicted in Figure 12. This picture shows that at least two different configurations can be realized in practice:

Two-wave (left panel (*a*)): when the main portion of the heavy fluid enters into the boundary layer ($\mu = 0.05$)

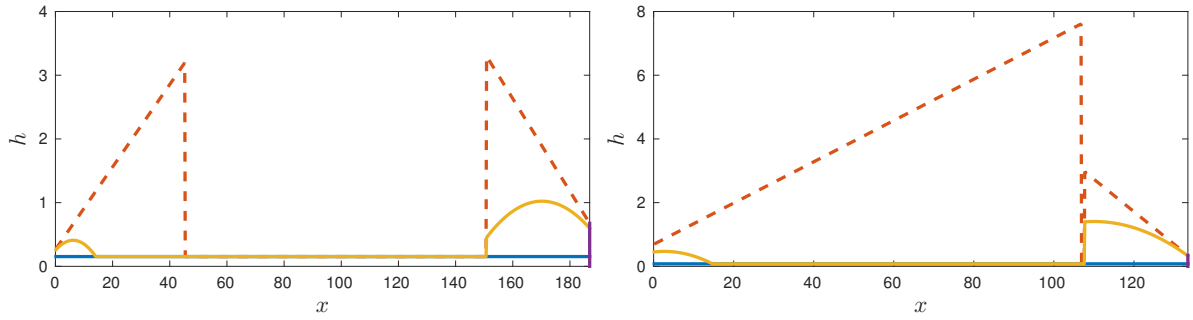

(a) $\mu = 0.05$ (b) $\mu = 0.654$

Figure 12. *Analytical solutions depicted at* $t_m = 50$ s. *All parameters are the same except for (a)* $\mu = 0.05$ *and (b)* $\mu = 0.654$. *The exact solutions are represented with dashed lines, while visible boundaries are shown with solid lines. Solutions are terminated at the right boundary by the vertical sharp front. Notice different vertical scales on left and right panels.*

One-wave (right panel (*b*)): when the flow in the buoyant jet reaches the head front ($\mu = 0.654$).

Remark 8. *In experiments in order to highlight the processes happening in the flow, the heavy fluid of density* ρ_0 *is in general coloured. Other experimental visualization techniques are also available, but the fluid painting is the most widely used one. By* ρ_a *we denote the density of the light ambient fluid. In such experimental conditions the* visible *interface between two fluids is located, where the following condition is satisfied:*

$$\rho_v - \rho_a \geqslant \varpi \cdot (\rho_0 - \rho_a),$$

where ρ_v *is the visible density and* ϖ *is a constant whose approximate value belongs to the segment* $[0.01, 0.1] \ni \varpi$. *For the sake of illustration, we depicted this visible interfaces in Figure 12 with solid lines, while the exact analytical solutions were shown with dashed lines. In the preparation of the visible interface we assumed that the fluid density varies linearly inside the turbulent layer from* ρ_a *to* ρ_0. *In other words, the virtual visible interface* $y = y_v$ *is determined by the following relation:*

$$\rho_v - \rho_a = (\rho_0 - \rho_a) \cdot \left(1 - \frac{y_v}{h}\right) = \varpi \cdot (\rho_0 - \rho_a).$$

For the sake of convenience, the last condition can be equivalently reformulated in terms of the buoyancy variable:

$$y_v(x) = \begin{cases} h(x) \cdot \left(1 - \varpi \dfrac{b_0}{b(x)}\right), & b(x) \geqslant \varpi b_0, \\ 0, & \text{otherwise.} \end{cases}$$

B. Derivation of the speed-Froude relation

From "boundary" conditions (3.28), (3.29) we deduce the following system of two equations with respect to unknowns u and c:

$$\begin{aligned} \left(u - c\right) + \tfrac{1}{2}\, m &= 0\,, \\ \left(c - u\right)^2 &= m\,. \end{aligned}$$

By solving this system we obtain the following solution ($u \neq 1$):

$$u = \tfrac{1}{3}\, c\,, \qquad m = \tfrac{4}{9}\, c^2\,.$$

Furthermore, by definition we have

$$\mathrm{Fr}_b = \frac{w_b}{\sqrt{m_b}}\,.$$

Thus,

$$U_b^3 = b_0\, \zeta_b\, w_b = m_b\, w_b = \mathrm{Fr}_b\, m_b^{3/2}\,.$$

Hence,

$$m_b^{1/2} = \mathrm{Fr}_b^{-1/3}\, U_b\,.$$

Taking into account the last results, the "boundary" condition (3.27) becomes:

$$m \cdot \left(c - u\right) + U_b^3 \cdot \left(\frac{c}{w_b} - 1\right) = 0\,.$$

Or equivalently we have:

$$m\left(c - u\right) U_b^{-3} + \left(c \cdot \mathrm{Fr}_b^{-1} \cdot m_b^{-1/2} - 1\right) = 0\,.$$

By rearranging the terms in the last equation we obtain:

$$\frac{8}{27}\, \frac{c^3}{U_b^3} + \mathrm{Fr}_b^{-2/3}\, \frac{c}{U_b} - 1 = 0\,.$$

By introducing the dimensionless velocity $C \overset{\text{def}}{:=} \frac{c}{U_b}$ we obtain the required Equation (3.30).

C. Nomenclature

In the main text above we used the following notations (this list is not exhaustive):

$\equiv$: equal identically

$\propto$: proportional

$\overset{\text{def}}{:=}$: the left hand side is defined

$\overset{\text{def}}{=:}$: the right hand side is defined

$\lesssim$: smaller than the approximate upper bound*

$\gtrsim$: greater than the approximate lower bound*

φ : angle of the bottom slope

α : local bottom slope, *i.e.* $\alpha = \tan\varphi$

h_j : total depth of the layer j

ρ_j : fluid density in the layer j

ζ : total depth of the bottom layer

b_j : buoyancy of the layer j

u_j : depth-averaged horizontal velocity of fluid particles in the layer j

v : vertical velocity component

w : transversal velocity component (in 3D)

p : fluid pressure

$m_j \stackrel{\text{def}}{:=} b_j h_j$: "mass" contained in the fluid column

$\mathcal{M}_j \stackrel{\text{def}}{:=} m_j u_j$: mass flux in the layer j

q : depth-averaged turbulent kinetic energy in the mixing layer

ξ : characteristics speed (*i.e.* eigenvalues of the JACOBIAN matrix of the hyperbolic fluxes)

$\lambda_{1,2}$: eigenvalues in the stability studies

π : volume fraction of heavy particles concentration

c : dimensional velocity of the travelling wave

C : dimensionless wave velocity

Fr : the dimensionless FROUDE number

ℓ, L : length scales

t : time variable

x : "horizontal" coordinate along the bottom slope

y : "vertical" coordinate normal to the bottom

$d(x)$: the bathymetry (depth) function

g : gravity acceleration

$\tilde{g}$: reduced gravity acceleration

χ : entrainment rate

u_* : friction velocity at the solid bottom

*We underline the fact that this bound is given approximatively.

References

[1] V. Alavian. Behavior of density currents on an incline. *Journal of Hydraulic Engineering*, 112(1):27–42, 1986. 15

[2] G. Alfonsi. Reynolds-Averaged Navier-Stokes Equations for Turbulence Modeling. *Applied Mechanics Reviews*, 62(4):40802, 2009. 12

[3] C. Ancey. Powder snow avalanches: Approximation as non-Boussinesq clouds with a Richardson number-dependent entrainment function. *J. Geophys. Res.*, 109:F01005, 2004. 8

[4] C. Ancey, S. Cochard, M. Rentschler, and S. Wiederseiner. Existence and features of similarity solutions for non-Boussinesq gravity currents. *Physica D*, 226:32–54, 2007. 8

[5] E. Audusse, M.-O. Bristeau, B. Perthame, and J. Sainte-Marie. A multilayer Saint-Venant system with mass exchanges for shallow water flows. Derivation and numerical validation. *ESAIM: Mathematical Modelling and Numerical Analysis*, 45(1):169–200, jun 2010. 8

[6] R. A. Bagnold. Experiments on a Gravity-Free Dispersion of Large Solid Spheres in a Newtonian Fluid under Shear. *Proc. R. Soc. A*, 225(1160):49–63, aug 1954. 10

[7] T. J. Barth and M. Ohlberger. Finite Volume Methods: Foundation and Analysis. In E. Stein, R. de Borst, and T. J. R. Hughes, editors, *Encyclopedia of Computational Mechanics*. John Wiley & Sons, Ltd, Chichester, UK, nov 2004. 40

[8] C. Beck, F. Manalt, E. Chapron, P. Van Rensbergen, and M. De Batist. Enhanced seismicity in the early post-glacial period: Evidence from the post-würm sediments of lake Annecy, northwestern Alps. *Journal of Geodynamics*, 22(1-2):155–171, 1996. 6

[9] P. Beghin, E. J. Hopfinger, and R. E. Britter. Gravitational convection from instantaneous sources on inclined boundaries. *J. Fluid Mech*, 107:407–422, jun 1981. 37

[10] F. Benkhaldoun, S. Sahmim, and M. Seaïd. Solution of the Sediment Transport Equations Using a Finite Volume Method Based on Sign Matrix. *SIAM J. Sci. Comput.*, 31(4):2866–2889, 2009. 7, 16

[11] F. Benkhaldoun, S. Sahmim, and M. Seaïd. A two-dimensional finite volume morphodynamic model on unstructured triangular grids. *Int. J. Num. Meth. Fluids*, 63(11):1296–1327, 2010. 16

[12] F. Benkhaldoun and M. Seaïd. Combined characteristics and finite volume methods for sediment transport and bed morphology in surface water flows. *Mathematics and Computers in Simulation*, 81(10):2073–2086, 2011. 7

[13] V. K. Birman, J. E. Martin, and E. Meiburg. The non-Boussinesq lock-exchange problem. Part 2. High-resolution simulations. *J. Fluid Mech.*, 537:125–144, 2005. 8

[14] V. Blagovechshenskiy, M. Eglit, and M. Naaim. The calibration of an avalanche mathematical model using field data. *Nat. Hazards Earth Syst. Sci.*, 2:217–220, 2002. 8

[15] R. T. Bonnecaze and J. R. Lister. Particle-driven gravity currents down planar slopes. *J. Fluid Mech*, 390:75–91, jul 1999. 19

[16] S. F. Bradford and N. D. Katopodes. Hydrodynamics of Turbid Underflows. I: Formulation and Numerical Analysis. *Journal of Hydraulic Engineering*, 125(10):1006–1015, 1999. 7

[17] P. Bradshaw, D. H. Ferriss, and N. P. Atwell. Calculation of boundary-layer development using the turbulent energy equation. *Journal of Fluid Mechanics*, 28(03):593–616, 1967. 15

[18] R. E. Britter and P. F. Linden. The motion of the front of a gravity current travelling down an incline. *J. Fluid Mech*, 99(03):531–543, aug 1980. 35, 36, 46

[19] D. L. Chapman. On the rate of explosion in gases. *Philosophical Magazine*, 47:90–104, 1899. 30

[20] E. Chapron, C. Beck, M. Pourchet, and J.-F. Deconinck. 1822 earthquake-triggered homogenite in Lake Le Bourget (NW Alps). *Terra Nova*, 11(2-3):86–92, 1999. 6

[21] E. Chapron, P. Van Rensbergen, M. De Batist, C. Beck, and J. P. Henriet. Fluid-escape features as a precursor of a large sublacustrine sediment slide in Lake Le Bourget, NW Alps, France. *Terra Nova*, 16(5):305–311, 2004. 6

[22] M. Chhay, D. Dutykh, M. Gisclon, and C. Ruyer-Quil. New asymptotic heat transfer model in thin liquid films. *Appl. Math. Model.*, In Press:1–24, mar 2017. 12

[23] S.-U. Choi and M. H. Garcia. Spreading of Gravity Plumes on an Incline. *Coastal Engineering Journal*, 43(04):221–237, dec 2001. 8

[24] T. De Luna, M. J. Castro-Diaz, and C. Parés Madroñal. Modeling and Simulation of Turbidity Currents. In *Finite Volumes for Complex Applications V*, pages 593–600. Wiley, 2008. 10

[25] F. Dias, D. Dutykh, and J.-M. Ghidaglia. A two-fluid model for violent aerated flows. *Comput. & Fluids*, 39(2):283–293, 2010. 11

[26] W. Dietrich. Settling Velocity of Natural Particles. *Water Resour. Res.*, 18(6):1615–1626, 1982. 11

[27] F. Dufour, U. Gruber, and W. Ammann. Avalanches: études effectuées dans la Vallée de la Sionne en 1999. *Les Alpes*, 2:9–15, 2001. 7

[28] D. Dutykh, C. Acary-Robert, and D. Bresch. Mathematical modeling of powder-snow avalanche flows. *Studies in Applied Mathematics*, 127(1):38–66, 2011. 8

[29] D. Dutykh, M. Chhay, and F. Fedele. Geometric numerical schemes for the KdV equation. *Comp. Math. Math. Phys.*, 53(2):221–236, 2013. 47

[30] D. Dutykh and D. Clamond. Modified shallow water equations for significantly varying seabeds. *Appl. Math. Model.*, 40(23-24):9767–9787, dec 2016.

[31] D. Dutykh, T. Katsaounis, and D. Mitsotakis. Finite volume methods for unidirectional dispersive wave models. *Int. J. Num. Meth. Fluids*, 71:717–736, 2013. 47

[32] H. A. Einstein. Formulas for the transportation of bed load. *American Society of Civil Engineers Transactions*, 107:561–577, 1952. 11

[33] T. H. Ellison and J. S. Turner. Turbulent entrainment in stratified flows. *J. Fluid Mech*, 6(03):423–448, mar 1959. 5, 12

[34] J. Etienne, E. J. Hopfinger, and P. Saramito. Numerical simulations of high density ratio lock-exchange flows. *Phys. Fluids*, 17:36601, 2005. 8

[35] J. Fe, L. Cueto-Felgueroso, F. Navarrina, and J. Puertas. Numerical viscosity reduction in the resolution of the shallow water equations with turbulent term. *Int. J. Num. Meth. Fluids*, 58:781–802, 2008. 8

[36] J. Fe, F. Navarrina, J. Puertas, P. Vellando, and D. Ruiz. Experimental validation of two depth-averaged turbulence models. *Int. J. Num. Meth. Fluids*, 60:177–202, 2009. 8

[37] I. Fer, U. Lemmin, and S. A. Thorpe. Contribution of entrainment and vertical plumes to the winter cascading of cold shelf waters in a deep lake. *Limnology*, 47(2):576–580, 2002. 6

[38] I. Fer, U. Lemmin, and S. A. Thorpe. Observations of mixing near the sides of a deep lake in winter. *Limonology And Oceanography*, 47(2):535–544, 2002. 33

[39] I. Fer, U. Lemmin, and S. A. Thorpe. Winter cascading of cold water in Lake Geneva. *Journal of Geophysical Research*, 107(C6):16, 2002. 6

[40] E. D. Fernandez-Nieto, F. Bouchut, D. Bresch, M. J. Castro-Diaz, and A. Mangeney. A new Savage-Hutter type models for submarine avalanches and generated tsunami. *J. Comput. Phys.*, 227(16):7720–7754, 2008. 7

[41] W. Fickett and W. C. Davis. *Detonation: Theory and Experiment*. University of California Press, Berkeley, CA, 1979. 30, 38, 45

[42] F. A. Forel. Les ravins sous-lacustres des fleuves glaciaires. *C. R. Ac. Sci. Paris§*, 101:725–728, 1885. 6

[43] Y. Fukushima and G. Parker. Numerical Simulation of Powder-Snow Avalanches. *Journal of Glaciology*, 36:229–237, 1990. 10

[44] M. Garcia and G. Parker. Experiments on the Entrainment of Sediment Into Suspension by a Dense Bottom Current. *J. Geophys. Res.*, 98(C3):4793–4807, 1993. 5, 6

[45] M. H. Garcia. Hydraulic Jumps in Sediment-Driven Bottom Currents. *J. Hydraul. Eng.*, 119(10):1094–1117, 1993. 15

[46] E. H. M. Georgeson. The Free Streaming of Gases in Sloping Galleries. *Proc. R. Soc. A*, 180(983):484–493, jul 1942. 35, 36, 46

[47] E. Godlewski and P.-A. Raviart. *Hyperbolic systems of conservation laws*. Ellipses, Paris, 1990. 23, 31, 40

[48] S. K. Godunov. A finite difference method for the numerical computation of discontinuous solutions of the equations of fluid dynamics. *Mat. Sb.*, 47:271–290, 1959. 40, 47

[49] S. K. Godunov. Reminiscences about Difference Schemes. *J. Comput. Phys.*, 153:6–25, 1999.

[50] S. K. Godunov and V. S. Ryabenkii. *Difference Schemes*. North-Holland, Amsterdam, 1987. 40, 47

[51] L. Gosse. *Computing Qualitatively Correct Approximations of Balance Laws: Exponential-Fit, Well-Balanced and Asymptotic-Preserving*, volume 2 of *SIMAI Springer Series*. Springer Milan, Milano, 1 edition, 2013. 47

[52] A. Grass. Sediment transport by waves and currents. Technical report, SERC London Cent. Mar. Technol., 1981. 11, 16

[53] F. F. Grinstein and G. E. Karniadakis. Alternative LES and Hybrid RANS/LES. *J. Fluids Eng.*, 124:821–942, 2002. 12

[54] C. J. Härtel, E. Meiburg, and F. Necker. Analysis and Direct Numerical Simulation of the Flow at a Gravity-current Head. Part 1. Flow topology and front speed for slip and no-slip boundaries. *J. Fluid Mech.*, 418(9):189–212, 2000. 8

[55] H. Helmholtz. On the discontinuous movements of fluids. *Monthly Reports of the Royal Prussian Academy of Philosophy in Berlin*, 23:215, 1868. 17, 24, 26

[56] E. J. Hopfinger. Snow avalanche motion and related phenomena. *Ann. Rev. Fluid Mech.*, 15:47–76, 1983. 7, 8

[57] H. Huang, J. Imran, and C. Pirmez. Numerical Model of Turbidity Currents with a Deforming Bottom Boundary. *J. Hydraul. Eng.*, 131(4):283–293, apr 2005. 8

[58] H. E. Huppert and J. E. Simpson. The slumping of gravity currents. *J. Fluid Mech*, 99(04):785–799, aug 1980. 7

[59] J. Imran, A. Kassem, and S. M. Khan. Three-dimensional modeling of density current. I. Flow in straight confined and unconfined channels. *J. Hydr. Res.*, 42(6):578–590, nov 2004. 8

[60] D. L. Inman, C. E. Nordstrom, and R. E. Flick. Currents in Submarine Canyons: An Air-Sea-Land Interaction. *Ann. Rev. Fluid Mech.*, 8(1):275–310, jan 1976. 6
[61] M. Ishii and T. Hibiki. *Thermo-fluid dynamics of two-phase flow*. Birkhäuser, 2006. 11
[62] C. G. Johnson and A. J. Hogg. Entraining gravity currents. *J. Fluid Mech.*, 731:477–508, sep 2013. 8, 12, 14, 38
[63] D. W. Jordan and P. Smith. *Nonlinear Ordinary Differential Equations: Problems and Solutions*. Oxford University Press, Oxford, 4 edition, 2007. 28
[64] A. Kassem and J. Imran. Three-dimensional modeling of density current. II. Flow in sinuous confined and uncontined channels. *J. Hydr. Res.*, 42(6):591–602, nov 2004. 8
[65] G. H. Keulegan. An experimental study of the motion of saline water from locks into fresh water channels. *U. S. Natl. Bur. Stand. J.*, page 5168, 1957. 12
[66] S. M. Khan, J. Imran, S. F. Bradford, and J. Syvitski. Numerical modeling of hyperpycnal plume. *Marine Geology*, 222-223:193–211, nov 2005. 7
[67] D. C. Krause, W. C. White, D. J. W. Piper, and B. C. Heezen. Turbidity currents and cable breaks in the western New Britain Trench. *Bull. Geol. Soc. Am.*, 81(7):2153–2160, 1970. 5
[68] Y. Kubo. Experimental and numerical study of topographic effects on deposition from two-dimensional, particle-driven density currents. *Sedimentary Geology*, 164(3-4):311–326, feb 2004. 6
[69] Y. Kubo and T. Nakajima. Laboratory experiments and numerical simulation of sediment-wave formation by turbidity currents. *Marine Geology*, 192(1-3):105–121, dec 2002. 6
[70] P. H. Kuenen. Density Currents in connection with the problem of Submarine Canyons. *Geological Magazine*, 75(06):241–249, jun 1938. 6
[71] H. Lamb. *Hydrodynamics*. Cambridge University Press, Cambridge, 1932. 10
[72] P. D. Lax. *Hyperbolic Systems of Conservation Laws and the Mathematical Theory of Shock Waves*. SIAM, Philadelphia, Penn., 1973. 22, 23, 31, 40, 46
[73] M. Lesieur. *Turbulence in Fluids*, volume 84 of *Fluid Mechanics and Its Applications*. Springer, 2008. 17, 23
[74] V. Y. Liapidevskii. Mixing Layer on the Lee Side of an Obstacle. *Journal of Applied Mechanics and Technical Physics*, 45(2):199–203, mar 2004. 8, 24, 25, 26
[75] V. Y. Liapidevskii and V. M. Teshukov. *Mathematical models of long wave propagation in an inhomogeneous fluid*. Izd. Sib. Otd. Ross. Akad. Nauk, Novosibirsk, 2000. 7, 14, 23, 25, 26, 27, 47
[76] D. K. Lilly. A Severe Downslope Windstorm and Aircraft Turbulence Event Induced by a Mountain Wave. *J. Atm. Sci.*, 35(1):59–77, jan 1978. 6
[77] P. L.-F. Liu. Turbulent boundary layer effects on transient wave propagation in shallow water. *Proc. Roy. Soc. London*, 462(2075):3481–3491, 2006. 15
[78] J. L. Lumley. A Century of Turbulence. *Advances*, 66(3):241–286, 2001. 12
[79] A. M. Lyapunov. *The General Problem of the Stability of Motion*. Doctoral dissertation, Kharkov University, Ukraine, 1892. 32
[80] S. Massel. *Ocean Waves Breaking and Marine Aerosol Fluxes*, volume 38 of *Atmospheric and Oceanographic Sciences Library*. Springer New York, New York, NY, 2007. 35
[81] T. Maxworthy. Experiments on gravity currents propagating down slopes. Part 2. The evolution of a fixed volume of fluid released from closed locks into a long, open channel. *J. Fluid Mech*, 647:27–51, mar 2010. 37

[82] Z. Mei, A. J. Roberts, and Z. Li. Modelling the dynamics of turbulent floods. *SIAM J. Appl. Math*, 63(2):423–458, 2003. 8

[83] E. Meiburg and B. Kneller. Turbidity Currents and Their Deposits. *Ann. Rev. Fluid Mech.*, 42(1):135–156, jan 2010. 6, 10

[84] Y. Meyapin, D. Dutykh, and M. Gisclon. Velocity and energy relaxation in two-phase flows. *Stud. Appl. Maths.*, 125(2):179–212, 2010. 8, 11

[85] E. Meyer-Peter and R. Muller. Formulas for bed load transport. In *Proceedings of the 2nd congress of the International Association for Hydraulic Research*, pages 39–64, 1948. 11, 16

[86] G. V. Middleton. Experiments on density and turbidity currents: III. Deposition of sediment. *Canadian Journal of Earth Sciences*, 4(3):475–505, 1967. 6

[87] B. Mohammadi and O. Pironneau. *Analysis of the K-Epsilon Turbulence Model*. John Wiley and Sons, 1994. 13

[88] T. Morales de Luna, M. J. Castro-Diaz, C. Pares Madronal, and E. D. Fernandez-Nieto. On a Shallow Water Model for the Simulation of Turbidity Currents. *Commun. Comput. Phys.*, 6:848–882, 2009. 7, 10, 16

[89] M. Naaim and I. Gurer. Two-phase Numerical Model of Powder Avalanche. Theory and Application. *Natural Hazards*, 117:129–145, 1998. 8

[90] F. Naaim-Bouvet. *Approche macro-structurelle des écoulements bi-phasiques turbulents de neige et de leur interaction avec des obstacles*. Habilitation à diriger des recherches, Cemagref, 2003. 10

[91] P. J. Neiman, R. M. Hardesty, M. A. Shapiro, and R. E. Cupp. Doppler Lidar Observations of a Downslope Windstorm. *Monthly Weather Review*, 116(11):2265–2275, nov 1988. 6

[92] P. Nielsen. *Coastal bottom boundary layers and sediment transport*, volume 4. World Scientific, 1992. 11, 16

[93] L. V. Ovsyannikov. Two-layer "Shallow water" model. *Journal of Applied Mechanics and Technical Physics*, 20(2):127–135, 1979. 10

[94] T. Özgökmen, P. F. Fischer, J. Duan, and T. Iliescu. Three-Dimensional Turbulent Bottom Density Currents from a High-Order Nonhydrostatic Spectral Element Method. *J. Phys. Ocean.*, 34:2006–2026, 2006. 8

[95] T. Özgökmen, T. Iliescu, P. F. Fischer, A. Srinivasan, and J. Duan. Large eddy simulation of stratified mixing in two-dimensional dam-break problem in a rectangular enclosed domain. *Ocean Modelling*, 16:106–140, 2007. 8

[96] H. M. Pantin. Interaction between velocity and effective density in turbidity flow: Phase-plane analysis, with criteria for autosuspension. *Marine Geology*, 31(1-2):59–99, apr 1979. 5, 7

[97] G. Parker. Conditions for the ignition of catastrophically erosive turbidity currents. *Marine Geology*, 46(3-4):307–327, apr 1982. 5

[98] G. Parker, Y. Fukushima, and H. M. Pantin. Self-accelerating turbidity currents. *J. Fluid Mech.*, 171:145–181, 1986. 5, 7

[99] J. D. Parsons, C. T. Friedrichs, P. A. Traykovski, D. Mohrig, J. Imran, J. P. M. Syvitski, G. Parker, P. Puig, J. L. Buttles, and M. H. Garca. The Mechanics of Marine Sediment Gravity Flows. In *Continental Margin Sedimentation*, pages 275–337. Blackwell Publishing Ltd., Oxford, UK, 2007. 6

[100] G. Pawlak and L. Armi. Vortex dynamics in a spatially accelerating shear layer. *J. Fluid Mech*, 376:1–35, dec 1998. 15, 24, 46

[101] G. Pawlak and L. Armi. Mixing and entrainment in developing stratified currents. *J. Fluid Mech.*, 424:45–73, dec 2000. 25, 26, 27, 38

[102] L. F. Pratson, J. Imran, E. W. H. Hutton, G. Parker, and J. P. M. Syvitski. BANG1D: a one-dimensional, Lagrangian model of subaqueous turbid surges. *Computers & Geosciences*, 27(6):701–716, jul 2001. 8

[103] M. Rastello and E. J. Hopfinger. Sediment-entraining suspension clouds: a model of powder-snow avalanches. *J. Fluid. Mech.*, 509:181–206, 2004. 7, 20, 39, 40, 41, 42, 43, 46

[104] E. V. Richardson. Sediment Transport. *Transport*, pages 46–57, 1985. 11

[105] A. N. Ross, S. B. Dalziel, and P. F. Linden. Axisymmetric gravity currents on a cone. *J. Fluid Mech*, 565:227–253, oct 2006. 19, 37, 38

[106] P. Sagaut. *Large eddy simulation for incompressible flows: an introduction*, volume 55 of *Scientific Computation*. Springer, 2006. 12, 13

[107] T. M. Salaheldin, J. Imran, M. H. Chaudhry, and C. Reed. Role of fine-grained sediment in turbidity current flow dynamics and resulting deposits. *Marine Geology*, 171(1-4):21–38, dec 2000. 8

[108] O. E. Sequeiros, H. Naruse, N. Endo, M. H. Garcia, and G. Parker. Experimental study on self-accelerating turbidity currents. *J. Geophys. Res.*, 114(C5):C05025, may 2009. 5

[109] K. R. Sreenivasan. Fluid turbulence. *Reviews of Modern Physics*, 71(2):S383–S395, 1999. 7, 12, 17, 23

[110] J. J. Stoker. *Water waves, the mathematical theory with applications*. Wiley, 1958. 10

[111] G. A. Tickle. A model of the motion and dilution of a heavy gas cloud released on a uniform slope in calm conditions. *J. Haz. Mat.*, 49(1):29–47, jul 1996. 19

[112] J. C. Tochon-Dangay. *Etude des courants de gravité sur forte pente avec application aux avalanches poudreuses*. Thèse, Université Scientifique et Médicale de Grenoble, 1977. 35, 36, 46

[113] A. A. R. Townsend. *The Structure of Turbulent Shear Flow*. Cambridge University Press, 2 edition, 1980. 7, 13, 15

[114] B. Turnbull, J. N. McElwaine, and C. Ancey. Kulikovskiy-Sveshnikova-Beghin model of powder snow avalanches: Development and application. *J. Geophys. Res.*, 112:F01004, 2007. 8

[115] J. S. Turner. *Buoyancy Effects in Fluids*. Cambridge University Press, 1973. 7, 11

[116] J. S. Turner. Turbulent entrainment: the development of the entrainment assumption, and its application to geophysical flows. *J. Fluid Mech*, 173:431–471, dec 1986. 19

[117] M. Ungarish. *An Introduction to Gravity Currents and Intrusions*. Chapman & Hall/CRC, Boca Raton, FL, 2009. 5

[118] I. R. Wood. Studies of unsteady self preserving turbulent flows. Technical report, Water Res. Lab., University of New South Wales (UNSW), Sydney, Australia, 1965. 35, 36, 46

[119] Y. B. Zel'dovich. On the theory of the propagation of detonation in gaseous systems. *JETP*, 10:542–568, 1940. 33

V. Liapidevskii: Novosibirsk State University and Lavrentyev Institute of Hydrodynamics, Siberian Branch of RAS, 15 Av. Lavrentyev, 630090 Novosibirsk, Russia
E-mail address: vliapid@mail.ru
URL: https://www.researchgate.net/profile/V_Liapidevskii/

D. Dutykh: LAMA, UMR 5127 CNRS, Université Savoie Mont Blanc, Campus Scientifique, F-73376 Le Bourget-du-Lac Cedex, France
E-mail address: Denys.Dutykh@univ-smb.fr
URL: http://www.denys-dutykh.com/

M. Gisclon: LAMA, UMR 5127 CNRS, Université Savoie Mont Blanc, Campus Scientifique, F-73376 Le Bourget-du-Lac Cedex, France
E-mail address: Marguerite.Gisclon@univ-smb.fr
URL: http://www.lama.univ-savoie.fr/~gisclon/